Performance Characterization of Electrohydrodynamic Propulsion Devices

by

Kento Masuyama

Submitted to the Department of Aeronautics and Astronautics
in partial fulfillment of the requirements for the degree of

Master of Science

at the

MASSACHUSETTS INSTITUTE OF TECHNOLOGY

September 2012

Author .....
Department of Aeronautics and Astronautics
August 23, 2012

Certified by .....
Steven R.H. Barrett
Assistant Professor
Thesis Supervisor

Accepted by .....
Eytan H. Modiano
Professor of Aeronautics and Astronautics
Chair, Graduate Program Committee

Performance Characterization of Electrohydrodynamic Propulsion Devices

by

Kento Masuyama

Submitted to the Department of Aeronautics and Astronautics
on August 23, 2012, in partial fulfillment of the
requirements for the degree of
Master of Science

Abstract

Partially ionized fluids can gain net momentum under an electric field, as charged particles undergo momentum-transfer collisions with neutral molecules in a phenomenon termed an ionic wind. Electrohydrodynamic thrusters generate thrust by using two or more electrodes to ionize the ambient fluid and create an electric field. In this thesis, electrohydrodynamic thrusters of single- and dual-stage configurations were tested. Single-stage thrusters refer to a geometry employing one emitter electrode, an air gap of length d, and a collector electrode with large radius of curvature relative to the emitter. Dual-stage thrusters add a collinear intermediate electrode in between the emitter and collector. Single-stage thruster performance was shown to exhibit trends in agreement with the one-dimensional theory under both positive and negative DC excitations. Increasing the gap length requires a higher voltage for thrust onset, generates less thrust per input voltage, generates more thrust per input current, and most importantly generates more thrust per input power. A thrust-to-power ratio as high as 68.43 mN/W was obtained for a $d = 21$ cm thruster. Dual-stage thrusters were shown to be more effective than its single-stage counterpart of equal total gap length at producing current, leading to a smaller total voltage necessary for producing equal thrust. However, losses involving ion collection at the intermediate electrode led to reduced thrust-per-power compared to the single-stage of equal length. A factor ψ was defined in order to characterize these losses, and the theoretical dependence of thrust-to-power on ψ was experimentally confirmed. A nondimensional quality term was derived, allowing for comparisons between the measured thrust-to-power values and the theoretical predictions.

Thesis Supervisor: Steven R.H. Barrett
Title: Assistant Professor

Acknowledgments

I would like to thank Steven Barrett for invaluable advice in supervising this work, Todd Billings and James Letendre for help in constructing the setup, and the Gas Turbine Laboratory for providing office and laboratory space. I would also like to thank the National Science Foundation Graduate Research Fellowship Program for helping to fund my education and research opportunities.

Contents

List of Figures

List of Tables

Chapter 1

Introduction and Theory

Electrohydrodynamic (EHD) thrusters are devices which convert electrical energy directly into a thrust force [4]. Every electrohydrodynamic device requires electrodes to create an electric field, an ion source, and an ambient fluid. EHD thrusters of various shapes and sizes have been built, but they have all included components comprising an asymmetric capacitor, namely two or more electrodes of different sizes and an air gap [3] [7] [10] [11] [20] [25]. These designs required no moving parts, suggesting possible thruster designs with little to no necessity for maintenance. Another advantage of EHD propulsion is the nonnecessity of stored propellants. Instead, the surrounding fluid is ionized and accelerated, meaning the exhaust consists only of ionized products of the local atmosphere. In a culture of growing concern for pollution and the environment, EHD exhaust introduces no pollutant species not already in the air. The cost is then the necessity for electrical power generation, as in the case of other electrical propulsion systems such as ion thrusters and Hall-effect thrusters. One possible implementation is on large blimps, whose large surface areas could be useful for electricity generation via solar cells [25]. Such vehicles may be useful in surveillance and communication, or perhaps even for exploring extraterrestrial bodies with dense atmospheres.

Electrohydrodynamics is the study of the interactions between electric fields and fluids. The first proposal for use in propulsion was made by Thomas Townsend Brown in the 1920s [4]. Brown hypothesized that the electric field was interacting with the

gravitational field in what he called the Biefield-Brown Effect. Subsequent tests have shown that the gravitational field is not involved, and that the thrust is produced by a phenomenon termed an ionic wind.

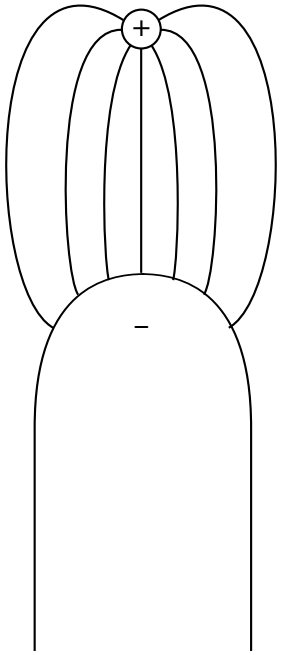

Figure 1-1: Asymmetrical capacitor and nonuniform electric field lines

An ionic wind is induced in a neutral fluid through interactions with ionized particles in an electric field. When a voltage is applied across an asymmetrical capacitor, in which the two electrodes have different radii of curvature, a nonuniform electric field is created as in figure 1-1. When the voltage increases beyond the corona inception voltage (V_o), the air around the smaller emitter electrode is ionized by the potential gradient, and ions are transported at the drift velocity towards the collector electrode. In vacuum, ions in an electric field would accelerate continuously until they collide with the collector; however, in air, they undergo collisions with neutral species, losing momentum with each collision. Macroscopically, these collisions appear as a drag force which acts opposite the electrostatic force, and charge is transported at an average drift velocity, given by

$$v_D = \mu E, \tag{1.1}$$

where μ is the ion mobility and E is the electric field strength. The ions, after drifting

across the air gap, are collected at the collector electrode and thus do not contribute to thrust. However, at every ion-neutral collision, momentum is transferred from the ions to the neutrals. These neutrals, unaffected by the electric field, escape the system with net momentum along the direction from the emitter to the collector, resulting in a thrust on the two electrodes.

An implementation of EHD thrusters known as a "lifter" has been popular amongst science students and hobbyists. Lifters, like the one shown in figure 1-2, are made of lightweight materials, such as balsa wood available in art stores, and electrodes made of wire and Aluminum foil. Powered by external power supplies, lifters generate enough force to counter their weight and lift off of the ground. However, these hobby projects are not documented, and the available experimental data is scarce.

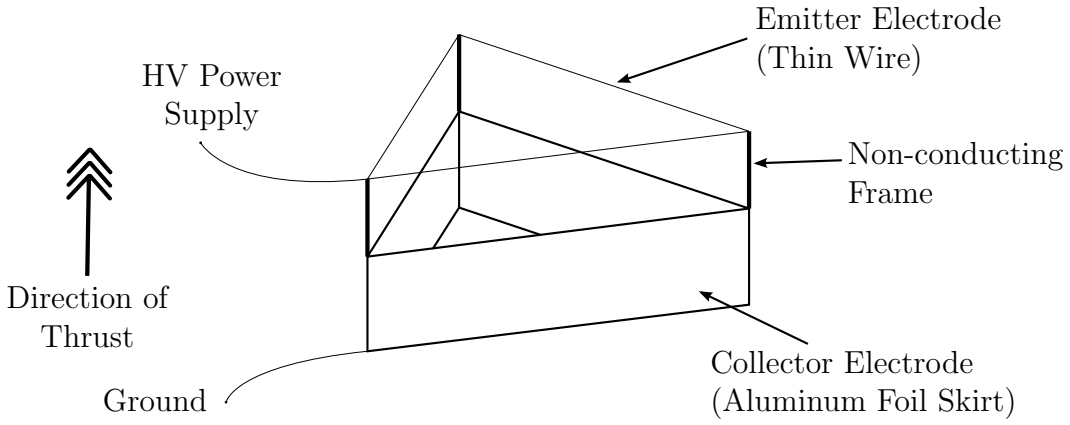

Figure 1-2: Example lifter

The purpose of this thesis was to characterize the performance of EHD thrusters. Data was collected for a single stage thruster, consisting of one emitter and one collector. Previous trends found in a study at the University of Cambridge by Barrett and Payton were confirmed, and a model for their behavior was explored. A dual stage design, which adds a third electrode allowing for finer tuning of the electric field, was tested in an effort to separate the two processes of ionization and acceleration.

The remainder of this chapter will discuss the underlying physics and theory. Chapter two will present a summary of previous works. Chapter three explains the methodology used in designing and testing both the single stage and dual stage thrusters. Chapter four presents the findings from the tests, as well as lessons learned

during the process. Chapter five gives the conclusions and areas requiring further study.

1.1 Corona Discharge Physics

As electrohydrodynamic thrusters have no onboard propellant, they rely on a corona discharge at the emitter electrode to provide ions. A corona is a nonuniform discharge which generates nonthermal, nonequilibrium plasma at atmospheric pressure. A corona discharge is ignited at the corona inception voltage, which is the lower threshold voltage for sustained current flow. The upper threshold of a stable discharge is when the field strength causes electrical breakdown of the surrounding fluid, at which point arcing occurs. In a "lifter" type EHD thruster, the electric field is created by a potential difference across the emitter and collector electrodes. The emitter electrode is designed with a significantly smaller radius of curvature than the collector, so that the field strength is stronger at the emitter than the collector. As such, the corona forms in the vicinity of the emitter.

An estimate of the critical field strength required to ignite the corona is given by the Peek formula [14]:

$$E_{cr} = 31\delta\left(1 + \frac{0.308}{\sqrt{\delta r}}\right), \tag{1.2}$$

where $\delta = \frac{3.92p}{T}$ with pressure p in cm Hg and temperature T in Kelvin, r is radius in cm, and E_{cr} is given in kV/cm. The Peek formula was empirically determined and is applicable to coaxial cylinders with inner radius between 0.01 to 1 cm and pressure 0.1 to 10 atm. Surface roughness on the electrodes, which effectively creates a locally reduced radius of curvature, can decrease the value by up to 20%. A different set of empirical constants can be used in the case of two parallel wires [14]:

$$E_{cr} = 30\delta\left(1 + \frac{0.301}{\sqrt{\delta r}}\right). \tag{1.3}$$

Equation 1.3 is likely a better fit for EHD thrusters due to the closer geometry.

The corona inception voltage V_o is then the voltage which, for the particular elec-

trode geometry, gives a maximum field value in excess of the critical field strength. Fridman and Kennedy give analytical expressions for the electric field in several geometries [14]. In particular,

$$E_{max} = \frac{V}{r \ln[\frac{d}{r\sqrt{1+(d/2b)^2}}]} \tag{1.4}$$

$$E_{max} = \frac{V}{r \ln(2b/r)} \tag{1.5}$$

$$E_{max} = \frac{V}{r \ln(d/r)} \tag{1.6}$$

where equation 1.4 is calculated for two parallel wires of radius r separated by a distance d, and both wires are a distance b from a conducting plane. Thus, equation 1.5 is the case $d \to \infty$ or a single wire parallel to a plane, and equation 1.6 is the case $b \to \infty$ or two parallel wires with no interacting plane. The electrode geometry for EHD thrusters is in between these latter two cases, so the two equations may be taken as the bounds for the actual value of V_o.

1.1.1 Corona Polarity

The polarity of the applied voltage can create positive or negative coronas. If the anode is the emitter, the plasma is a positive corona; if the cathode is the emitter, the plasma is a negative corona. The mechanisms by which continuous ionization is maintained differ between the two polarities, leading to different properties [14].

Figure 1-3: Positive corona discharge

Coronas of either polarity are first ignited by an external ionization event, such as excitation by ultraviolet photons or radio frequency waves, which creates a primary electron. In the case of a positive corona, this electron is attracted by the strong

potential gradient towards the emitter, leading to ionizing collisions with neutrals and starting an electron avalanche. Within the resulting plasma, de-excitation events release photons causing a weak glow. These photons, which may manifest as cathode-directed streamers, then cause further ionization events in the neutral air surrounding the plasma, starting a series of secondary electron avalanches. Positive ions created in the avalanches and ionization events are repelled away from the emitter, eventually exiting the active region and starting its drift towards the collector. The resulting positive corona is uniform along the length of the emitter, as seen in figure 1-3.

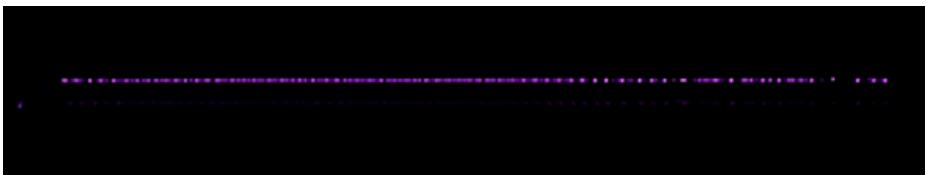

Figure 1-4: Negative corona discharge

In the case of a negative corona, the primary electron released by the initial external ionization event is accelerated away from the emitter, again starting an electron avalanche. However, these primary electrons are less energetic than in the positive case, as they are accelerated outwards into a lower potential gradient rather than inwards. Secondary electron avalanches are then created not by electrons accelerating into the active region, but rather by photons and positive ions colliding with the emitter itself, emitting secondary electrons outwards by the photoelectric effect. Electrons which escape the plasma combine with electronegative molecules such as O_2 and H_2O to form negative ions, which drift towards the collector. Negative coronas tend to appear as patches, seen in figure 1-4.

1.1.2 Ozone Production

Corona discharges produce ozone (O_3) as a byproduct. Many commercial and industrial ozone generators use corona discharge tubes for ozone production [17]. There are health risks associated with ozone that must be considered. Excessive exposure to ozone has been associated with respiratory diseases, and its strong oxidizing proper-

ties make it an irritant. Ozone also acts as a greenhouse gas in the upper atmosphere. Due to its potential harm, ozone is regulated by organizations including the Environmental Protection Agency [2], the Federal Aviation Administration [1], and the U.S. Occupational Safety and Health Administration [19].

Ozone is also known to degrade materials including rubber and plastic. Any experimental setup must then take care to limit exposure of such components to the produced ozone. Of particular concern is the degradation of wire insulation, which will allow for more ionization around the exposed wire and increased ozone production.

1.2 Thrust

The thrust produced by electrohydrodynamics is equal and opposite to the force acting on the fluid. A one dimensional theoretical model was derived for single- and dual-stage thrusters.

1.2.1 Single Stage Thruster

This derivation follows the same arguments as given by Payton [20]. Refer to diagram 1-5 for the terms relating to electrode geometry.

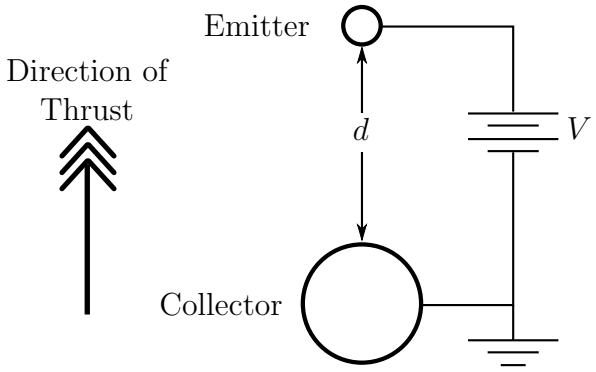

Figure 1-5: Single stage thruster electrode geometry

In order to find the expression for the force acting on the fluid, the following assumptions are made:

1. The electrodes are long relative to the gap length and the electrode radii ($L \gg d$, with L the length of the electrode out of the page),

2. The electric field in the gap is uniform and one dimensional,

3. The emitter is at a potential V,

4. The collector is grounded, $V_{collector} = 0$,

5. The current is low enough that space charge effects do not significantly disturb the current output or electric field.

The assumptions on electrode geometry and voltages can be controlled via experimental design. The space charge effect will be low at the onset of the corona discharge, but will become more pronounced as the current and hence charge density increase.

Gauss's Law in differential form is

$$\nabla \cdot E = \frac{\rho}{\epsilon_o}, \tag{1.7}$$

where ρ is charge density and $\epsilon_o \approx 8.854 \times 10^{-12}$ F/m is the permittivity of vacuum. As the relative permittivity of air is approximately 1, the value need not be changed for a thruster operating in air. Assuming the absence of a time-dependent magnetic field, by Faraday's Law,

$$\nabla \times E = -\frac{\partial B}{\partial t} = 0. \tag{1.8}$$

This allows for the definition of the electric field as

$$E = -\nabla\phi = -\frac{d\phi}{dx}, \tag{1.9}$$

where ϕ is electric potential and x is distance, measured from the emitter towards the collector. Substituting this back into equation 1.7, the familiar electrostatic Poisson's

equation is found:

$$\nabla \cdot E = \nabla \cdot (-\nabla \phi) = -\nabla^2 \phi = \frac{\rho}{\epsilon} \tag{1.10}$$

$$\nabla^2 \phi = -\frac{\rho}{\epsilon}. \tag{1.11}$$

In the case of uniform field as given in the assumptions, the electric field is given by

$$E = \frac{V}{d}. \tag{1.12}$$

Defining current density using the drift velocity given by equation 1.1 and defining a characteristic area A describing the area perpendicular to x occupied by ions,

$$j = \rho v_D = \rho \mu E \tag{1.13}$$

$$I = \int_S j \cdot dA = \rho \mu E A. \tag{1.14}$$

Solving for charge density,

$$\rho = \frac{I}{\mu E A} = \frac{Id}{\mu V A}. \tag{1.15}$$

Finally, solving for the Coulomb electrostatic force on the volume of ions occupying the gap at any instant in time,

$$F = \int_V \rho E dV = \int \rho E A dx = \int \frac{Id}{\mu V A} \frac{V}{d} A dx = \frac{Id}{\mu}. \tag{1.16}$$

The use of this steady-state drift velocity in the above steps requires that the electrostatic force on the ions equals the drag force created by ion-neutral collisions. This drag force is equal and opposite to the force on the neutral fluid, which itself is equal and opposite the thrust felt by the thruster. Thus, electrohydrodynamic thrust is expressed as

$$F = \frac{Id}{\mu}. \tag{1.17}$$

With many power supplies, the user sets the voltage and the corresponding current is drawn. As such, it may be of interest to find the thrust expression in terms of

voltage as opposed to current. The total current output from a corona discharge is approximated by

$$I = CV(V - V_o) \tag{1.18}$$

where C is a different constant for each particular geometry [14]. Substituting into the thrust equation, this gives

$$F = \frac{CV(V - V_o)d}{\mu}. \tag{1.19}$$

Cooperman obtained an empirical formula for C in the case of a wire parallel to a flat plate [12],

$$C = \mu \frac{2\pi\epsilon_o L}{d^2 \ln(\frac{f_{geo}}{r})}, \tag{1.20}$$

where L is the plate length, r is the wire radius, and f_{geo} is an empirical geometric factor. Substituting C into equation 1.19 and accounting for the d^2 term in the denominator as well as the ion mobility μ results in the relationship

$$F = \frac{C'V(V - V_o)}{d}, \tag{1.21}$$

where C' is the expression given by Cooperman with the μ and d^2 terms factored out.

From equations 1.17 and 1.21, the relationship between current, voltage, and force can be seen. The gap distance d is set by geometry and can be considered constant. The ion mobility μ varies with pressure, temperature, and humidity, but is not affected by the thruster operation and thus can also be considered constant. As such, the thrust is expected to vary linearly with current, and quadratically with voltage.

1.2.2 Dual Stage Thruster

The electric field created by the thruster electrodes serves two purposes: to ionize neutral air particles and to accelerate the resulting ions in order to produce a thrust force. As seen in equation 1.17, the force is proportional to both the current and the

gap distance. The current is set by the electrode geometry. However, it is hypothesized that by adding a third electrode collinear with the emitter and collector as shown in figure 1-6, the distance traveled by the ions can be increased without significant effect on the corona characteristics. Namely, there is one gap with separation d_1 responsible for creating a field strong enough to generate ions. There is a second gap of separation d_2 which will also create a field; however, this field will be below the corona inception threshold so that no additional ionization occurs. Ions created in the first gap will drift towards the intermediate electrode, but instead of all ions being collected there, some will continue to be accelerated by the field in the second gap to the collector electrode.

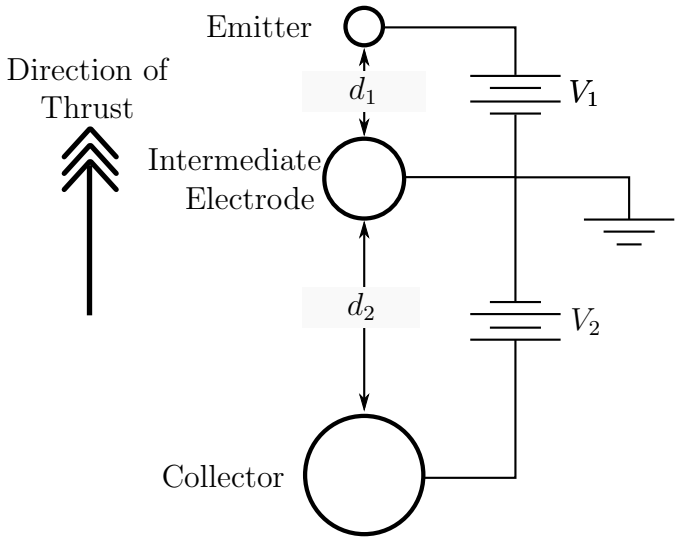

Figure 1-6: Dual stage thruster electrode geometry

In order to facilitate the maintenance of corona characteristics and the prevention of further ionization in the second gap, the intermediate electrode will be significantly larger than the emitter. A radius similar to the collector will produce electrical properties similar to the single stage thrusters, but an intermediate electrode larger than the collector will pose a large area of interference to the ionized particles and ionic wind, resulting in losses. The points described thus far can be summarized by these assumptions:

1. All ionization occurs at the emitter electrode,

2. A fraction of the current is collected at the intermediate electrode,

3. The remaining ions are collected at the collector.

As long as the thruster operates within these boundaries, the resulting thrust can be expressed as a variation of the single-stage case, equation 1.17. Following a similar argument as before, the electric field and charge densities are defined for each gap as

$$E_1 = \frac{V_1}{d_1} \qquad E_2 = \frac{V_2}{d_2} \tag{1.22}$$

$$\rho_1 = \frac{I_1}{\mu E_1 A} \qquad \rho_2 = \frac{I_2}{\mu E_2 A}. \tag{1.23}$$

From the assumption, all ions are produced at the emitter and collected at either the intermediate electrode or the collector. Defining a factor ψ with a value between 0 and 1 as the fraction of current which flows beyond the intermediate electrode across the second gap, the currents are related as $I_2 = \psi I_1$. The charge density and electric fields however are different in the two gaps, and thus are integrated separately:

$$F_{DS} = \int_{d_1} \rho_1 E_1 A dx + \int_{d_2} \rho_2 E_2 A dx = \frac{I(d_1 + \psi d_2)}{\mu}. \tag{1.24}$$

This result suggests that by adding in a third electrode, the thrust for a given current I_1 can be increased by a factor $(1 + \psi \frac{d_2}{d_1})$.

1.3 Performance Comparison

In order to characterize EHD thruster performance and develop metrics for design purposes, a basis for comparison must be established. Efficiency is a convenient metric to consider, but it must be defined appropriately. Overall efficiency can be separated into two components, the propulsive efficiency and thermal efficiency. Propulsive efficiency is the effectiveness of converting the energy of the exhaust or jet into aircraft power (thrust times velocity). In static tests, this term is zero as the thruster does not have a nonzero velocity. The thermal component is the efficiency of converting

input power into jet power in the exhaust,

$$\eta_{th} = \frac{P_{jet}}{P_{in}} = \frac{\frac{1}{2}\dot{m}c^2}{P_{in}} = \frac{Fc}{2P_{in}}, \tag{1.25}$$

where $P_{in} = IV$ is the electrical power supply output. In the jet power, $\dot{m}$ is the exhaust mass flow rate and c is the exhaust velocity. In order to calculate the efficiency, the experimental setup would be required to measure thrust, exhaust velocity, voltage, and current. Accurate measurement of exhaust velocity in EHD flow is difficult for two major reasons: the velocity profile is nonuniform and varies with operating voltage, and the flow properties are not compatible with common velocity measurement techniques [21]. EHD flow generates velocities on the order of 1 m/s, and the resulting pressure differential is too small to ensure accurate Pitot tube measurements. The charged species in the flow make velocimetry difficult, as the seed particles may gather charge and deviate from the streamlines under the electric field.

Looking again at overall efficiency, it can be expressed as the power applied on the thruster and aircraft divided by the input power, or

$$\eta = v\frac{F}{P}, \tag{1.26}$$

where v is the velocity. This efficiency is equal to zero due to the static test, but the remaining term $^{F}/_{P}$, or the thrust-to-power ratio, can be an effective performance metric. EHD thrusters have documented thrust-to-power ratios as high as 26 mN/W, which is orders of magnitude greater than electrostatic propulsion systems used in space and in excess of that for a typical jet engine at $\approx$ 15 mN/W [20]. Helicopters typically have values in the 40 - 75 mN/W range [27] [28].

Using the expressions derived earlier for thrust, it is possible to obtain expressions for this ratio as well. In the case of a single stage thruster,

$$\frac{F}{P}_{SS} = \frac{Id}{\mu IV} = \frac{d}{\mu V}. \tag{1.27}$$

In the case of the dual stage thruster, with the continued use of the assumption that

some current flows through the intermediate electrode, the input power is $I(V_1 + \psi|V_2|)$. As such, the ratio is seen to be

$$\frac{F}{P}_{DS} = \frac{I(d_1 + \psi d_2)}{\mu I(V_1 + \psi|V_2|)} = \frac{d_1 + \psi d_2}{\mu(V_1 + \psi|V_2|)}. \tag{1.28}$$

This expression can be expanded in ψ to see how the current distribution between the two gaps affects performance. Expanding to first order,

$$\frac{d_1 + \psi d_2}{\mu(V_1 + \psi|V_2|)} = \frac{d_1 + d_2}{\mu(V_1 + |V_2|)} + \frac{(\psi - 1)(d_2 V_1 - d_1|V_2|)}{\mu(V_1 + |V_2|)^2} + O(\psi^2). \tag{1.29}$$

The first term on the right hand side is positive, and the effect of ψ is seen in the second term. The denominator is positive, so looking at the numerator, it can be reformulated as

$$(\psi - 1)(d_2 V_1 - d_1|V_2|) = (1 - \psi)d_1|V_2|\left(1 - \frac{E_1}{E_2}\right). \tag{1.30}$$

Since $0 \leq \psi \leq 1$ and $E_1 > E_2$, the expression is negative. As such, a larger value of ψ, corresponding to a larger proportion of the current continuing past the intermediate electrode to the collector, minimizes the loss and is expected to generate a higher thrust-to-power ratio.

This ratio is dimensional and may be more subject to geometric dependence than the nondimensional efficiency. However, as seen in both expressions for single- and dual-stage thrusters, there is no need to measure flow velocity, thus reducing a potential source of error.

The thrust-to-power ratio dependence can also be derived from dimensional analysis. Looking at the dimensionality of $^F/_P$, it is seen to have units of [s/m]. This can be expressed as

$$\frac{F}{P}\ [\text{s/m}] = f(d\ [\text{m}], \mu\ [\text{m}^2/\text{Vs}], V\ [\text{V}]). \tag{1.31}$$

Application of dimensional analysis leads to

$$\frac{F\mu V}{Pd} = \text{ constant} \tag{1.32}$$

$$\frac{F}{P} \propto \frac{d}{\mu V}. \tag{1.33}$$

The nondimensional term on the left of equation 1.32 may be thought of as a metric for the quality of the configuration. It is a comparison of the experimental thrust-to-power ratio to the theoretical prediction:

$$\Omega_{SS} = \frac{\frac{F}{P}_{SS,experimental}}{\frac{F}{P}_{SS}} = \frac{{}^{F}/_{P}}{{}^{d}/_{\mu V}} = \frac{F\mu V}{Pd}. \tag{1.34}$$

For the dual-stage quality, the experimental thrust-to-power ratio is compared to the theoretical value given in equation 1.28 with ψ set to 1. The quality term is an attempt to compare to the theoretical ideal, so any losses involved in current loss at the intermediate electrode should be reflected in the value. As such,

$$\Omega_{DS} = \frac{F\mu(V_1 + V_2)}{P(d_1 + d_2)}, \tag{1.35}$$

and in general,

$$\Omega = \frac{F\mu V_{tot}}{Pd_{tot}}. \tag{1.36}$$

1.3.1 Bilinear Performance Degradation

In previous findings by Payton [20], an unexplained performance degradation was seen in the single stage thrust as a function of current. As seen in equation 1.17, the thrust is expected to be linear in current. However, as the current increases beyond some threshold, the slope decreases as shown in figure 1-7.

It is hypothesized that as the applied voltage is increased, a second corona discharge is ignited at the collector electrode. This corona is of the opposite polarity to that at the emitter, and will thus produce ions of the opposite charge. By separating the definition of current to include both components, it is possible to derive an

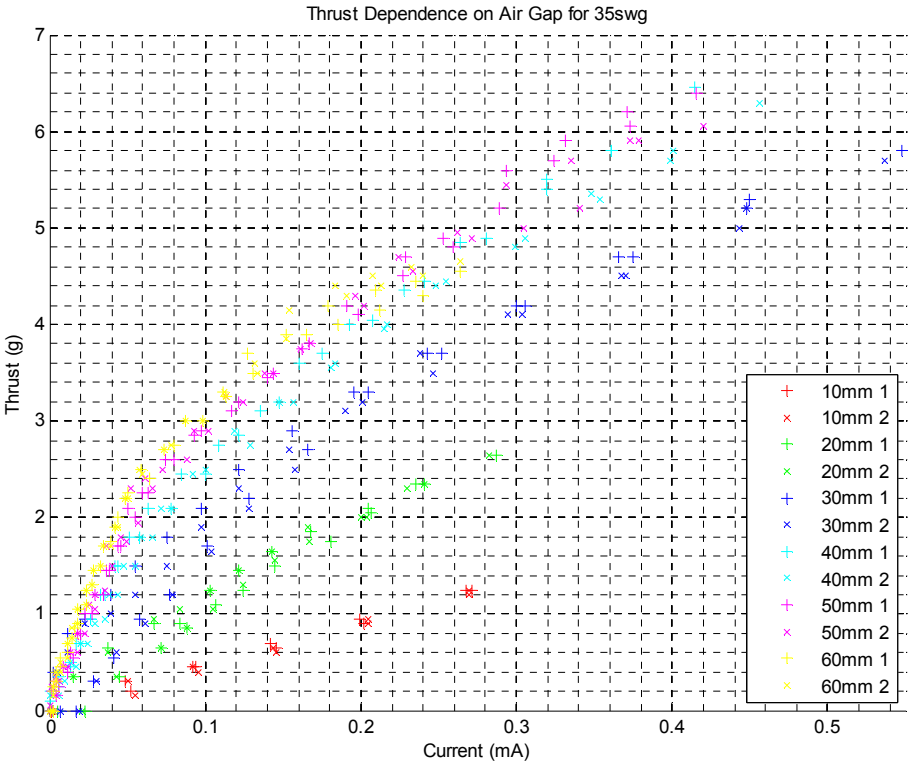

Figure 1-7: Thrust dependence on current (adapted from Payton [20])

expression for the thrust-to-power ratio for this degraded performance regime. The total current I is the sum of the two opposite ion flows,

$$I = I^+ + |I^-|. \tag{1.37}$$

The superscript $^+$ signifies the initial current and the superscript $^-$ the reverse current. Following the same derivation as before, the force in this regime consisting of both currents is

$$F = d\left(\frac{I^+}{\mu^+} - \frac{|I^-|}{\mu^-}\right). \tag{1.38}$$

Now defining the ratio of positive to negative ion mobilities as $\alpha = \frac{\mu^+}{\mu^-}$, the force in equation 1.38 can be rewritten as

$$\frac{d}{\mu^+}(I^+ - \alpha|I^-|) = a_2 I \tag{1.39}$$

where a_2 is the slope of the reduced performance regime in the thrust vs current plot. Similarly, the initial slope in this plot is defined as

$$a_1 = \frac{d}{\mu^+}. \tag{1.40}$$

Using the expanded definition of current,

$$a_2 \frac{\mu^+}{d} = A = \frac{I^+ - \alpha|I^-|}{I^+ + |I^-|}. \tag{1.41}$$

Now it is possible to find an expression for $|I^-|$ in terms of the slopes, ion mobilities, and overall current I. Starting with a system of equations using 1.37 and 1.41,

$$\begin{cases} AI &= I^+ - \alpha|I^-| \\ I &= I^+ + |I^-| \end{cases} \tag{1.42}$$

$$|I^-| = \frac{1-A}{1+\alpha} I = \frac{1 - a_2 \frac{\mu^+}{d}}{1 + \frac{\mu^+}{\mu^-}} I = \frac{1 - \frac{a_2}{a_1}}{1 + \frac{\mu^+}{\mu^-}} I. \tag{1.43}$$

Substituting equations 1.37 and 1.38 into 1.27,

$$\frac{F}{P} = \begin{cases} \frac{d}{\mu^+ V} & , V_o < V < V_{o2} \\ \frac{d}{V} \frac{\frac{I^+}{\mu^+} - \frac{|I^-|}{\mu^-}}{I^+ + |I^-|} & , V_{o2} < V \end{cases}. \tag{1.44}$$

This second equation can be simplified using the above expression for $|I^-|$, to be in terms of the two slopes:

$$\frac{d}{V} \frac{\frac{I^+}{\mu^+} - \frac{|I^-|}{\mu^-}}{I^+ + |I^-|} = \frac{d}{V} \frac{\frac{I}{\mu^+} - \frac{|I^-|(1+\alpha)}{\mu^+}}{I} = \frac{d}{\mu^+ V} \frac{a_2}{a_1} = \left(\frac{F}{P}_{SS}\right) \frac{a_2}{a_1}. \tag{1.45}$$

This same equation is also found by noting that $a_2 = \frac{F}{I}$ in the degraded regime and substituting that into $\frac{F}{IV}$.

If this bilinear performance model is in agreement with the data, it gives a better understanding of why EHD thruster performance decreases at higher thrust. This

information can then be used to better design the electrode geometry and mitigate this performance degradation mechanism.

Chapter 2

Previous Work on EHD Thrusters

Electrohydrodynamics was first proposed as a possible thrust mechanism by graduate student Thomas Townsend Brown in the 1920s. Although Brown produced no academic papers on the work, a series of US and GB patents were issued over the next several decades, starting with GB300311 [4]. Bahder and Fazi have described in detail the history of these patents and the developments that seem to have taken in terms of understanding the underlying physics throughout that time [3]. The discovery of the force, then called the Biefeld-Brown Effect, was made during experimentation on Coolidge tubes. The mechanism responsible for the force was not well understood, as can be seen in Brown's patent referencing a coupling of electromagnetism and gravity. By the late 1950s, Brown had conceived of the "lifter" design, as indicated by the included sketches in a 1960 patent [5]. Brown had made several key observations, although some have since then been shown false:

1. Raising the small electrode to positive voltage produces the greatest force

2. The effect can function as both a propulsive device or a pump for dielectric fluid

3. The effect is seen in dielectric medium, but the force is not reduced to zero in vacuum [6].

2.1 Early Studies

The concept of electric wind, or the net motion of a slightly ionized gas under electric field, was considered by Cheng in a 1961 Office of Naval Research paper [9]. Cheng used a one-dimensional model consisting of the aforementioned electric wind as well as electric pressure. The model yielded a relationship between thrust and ambient gas pressure, namely that thrust varied as p^2. This finding suggested that Brown's claim of a Biefeld-Brown thrust in vacuum is false, and that any application in space would require stored propellant. Another key finding was that within the realm of glow discharges, an abnormal glow discharge produces larger thrust per unit discharge area but the optimum operation point would be a glow discharge covering the entire electrode, due to its smaller specific power consumption. However, it was concluded that the glow discharge has limited potential as a primary propulsion device due to the lack of electrical power supplies with a high enough specific power.

In 1967, Christenson and Moller of U.C. Davis published a paper on EHD propulsion [10]. In this work, a one-dimensional analytical model was developed with results similar to that presented in the theory section. This model, consisting of two parallel electrode surfaces with the emitter featuring numerous sharp points, assumed a ducted fan flow. Christenson started with the Navier-Stokes equation assuming incompressible and inviscid flow. The resulting expression for thrust-to-power, with variables remapped to fit this paper, was

$$\frac{F}{P_{in}}_{CM} = \frac{d}{V}\frac{1}{\mu(1+\phi)}. \tag{2.1}$$

This equation has an additional factor of $(1+\phi)$ compared to equation 1.27. $\phi = \sqrt{\frac{2\epsilon}{\rho\mu^2}}$ is treated as a constant for a particular gas, with value $\phi \approx 0.02$ for air. This change is a result of differences in the definition of current density. Christenson's definition of current density included not just the ion drift velocity but also the induced velocity in the neutral gas:

$$j' = \rho(\mu E + u). \tag{2.2}$$

Redefining the current density in the derivation of 1.27 gives the expression

$$\frac{F'}{P} = \frac{d}{\mu V} \frac{1}{1 + \frac{u}{\mu E}}. \tag{2.3}$$

The term $\frac{u}{\mu E}$ has the same dimensionality as Christenson's ϕ, supporting the agreement between the two derivations. Due to its small value in the face of the simplifications made in the derivation, it is assumed safe in this present study to neglect this factor.

Christenson also conducted a series of experiments to verify the theory. The emitter consisted of sharp pointed aluminum rods attached in an area-weighted distribution to a series of concentric rings. The collector was another series of concentric rings with the upper surfaces rounded off, with maximum diameter of 1.167 ft. The two electrodes were mounted with clamps so that the gap distance could be adjusted. The results of the experiments confirmed the current density dependence $j \propto V(V - V_o)$. The relation of the thrust-to-power ratio was also tested and was seen to be bracketed by theoretical predictions using ion mobility values for saturated and dry air. Velocity measurements were taken with a bridled-vane-type air velocity meter as well as a hot-wire anemometer. Velocity profiles at 2.5, 6, and 11 in. below the collector supported the ducted-fan-type flow, with negligible flow entrainment. The energy or power efficiency was calculated to be on the order of 1%, in agreement with Goldman's results [15]. Finally, the energy efficiency was seen to be approximately proportional to the parameter ϕ.

2.2 Conflicting Ideas on Thrust Mechanism

Around the 1960s, "lifters" gained popularity amongst hobbyists, in part due to articles in popular magazines such as de Seversky's "Ionocraft" in a 1964 *Popular Mechanics* [13]. With a larger number of people working on EHD thrusters, other hypotheses were raised about the nature of the thrust production. One popular idea was the recoil force from ions being accelerated by the emitter. This idea, assuming

a ballistic trajectory for the charges, neglected the force in the opposite direction created by ion collisions with the collector. Bahder and Fazi at the Army Research Laboratory conducted a mathematical analysis to study the merits of this hypothesis [3]. By looking at the upper limit on the thrust assuming no force on the collector, they concluded that the recoil force would still be at least three orders of magnitude smaller than that observed in experiments. A scaling estimate was made for the ion drift theory, such as that employed by Christenson and Moller, showing that to within an order of magnitude, these models were plausible. The final model studied by Bahder and Fazi was a thermodynamic model of the fluid dielectric as acted upon by an external electric field. The derived expression for thrust consisted of four terms, including the familiar ρE force. The other three terms were dependent on the dielectric constant ϵ or its gradient; however, as the relative magnitudes of the four terms could not be estimated, this thermodynamic theory was not able to be verified.

Another theory had its roots in T. T. Brown's claim of a force even in vacuum. In a study for the Phillips Laboratory under the Air Force Systems Command Propulsion Directorate, Talley conducted a series of tests on asymmetric capacitors in a vacuum chamber [23]. Under conditions of high vacuum, up to 5.0×10^{-7} torr, no thrust was detected. However, two anomalous forces were observed upon electrical breakdown, which led to the hypothesis of a five-dimensional coupling between the gravitational and electromagnetic fields. In an effort to verify this coupling, Tajmar conducted an experiment utilizing a cylindrical EHD thruster suspended inside a hanging box [22]. Thrust due to electric wind would cause an oscillation of the setup, whereas a five-dimensional coupling would lead to a steady displacement of the box. Within the measuring accuracy of the setup, no such coupling was observed.

Canning, in a study of asymmetrical capacitor thrusters for NASA, also studied alternative theories for thrust production [8]. The first theory analyzed was ablation of the emitter electrode and the subsequent ejection of the ablated mass. By calculating the necessary mass ablation rate from the thrust and flow velocity, it was shown that the emitter could not have survived the amount of testing conducted. The second theory was electrostatic interaction with a conducting ground in the form of

image charges. However, this was qualitatively rejected as it would necessarily be an attractive force, leading to a downward force contrary to the lifting seen in previous experiments. The final theory was the ion drift picture as studied previously. The numbers predicted by this model agreed with their experimental measurements, using a setup consisting of two cylindrical asymmetric capacitors spinning around a vertical axis. The experiments were also conducted in several different conditions, including reduced pressure, pure Nitrogen, and pure Argon. Forces were seen in all cases, although weaker than in standard pressure air. The results were also summarized in an AIAA conference presentation [7].

2.3 Recent Work

Models to this point have mostly used one dimension for simplicity. Zhao created a computer simulation based on boundary and finite element methods as well as the method of characteristics to compute the two dimensional electric field, or the equivalent of infinitely long electrodes [26]. Furthermore, the airflow was computed in FLUENT. The model was based on the "lifter" design, with an emitter wire (circle) and a collector foil. The simulation assumed that the force is entirely due to the ion drift. The electric field was calculated on a mesh, and the resulting forces plugged into the FLUENT gas flow as body forces. This allowed for the calculation of both velocity and pressure distributions. Three forces were also calculated, the Coulomb force, the viscous drag, and the pressure forces.

In 2009, researchers from the Sandia National Laboratories contributed a chapter on EHD thrusters to an AIAA book on propulsion [18]. In this work, a "lifter" type thruster was constructed and tested under both DC and AC excitement. Under DC excitation, it was found that the polarity of the voltage did not affect performance. It was also seen that there was no dependence on small geometry changes. Finally, insulating the emitter wire using a coat of gryptol was shown to decrease the thrust, even when equal current was flowing. Under AC excitement, it was noted that the forces were nearly identical to the DC case. Similarly, varying the frequency of the

sinusoidal voltage showed little effect on the force. An interesting observation was that the point of maximum power consumption did not correspond to the maximum thrust. The effects of variations in the geometry were studied under AC excitation. For a given voltage, a smaller gap distance resulted in larger force. There was also a small local maximum for gaps in the 45 to 50 mm range, the exact gap depending on the operating voltage. The plate depth, or height of the foil, was shown to have no effect on the thrust, which suggests a smaller foil for mass savings. Aside from DC and AC excitation, the effects of a magnetic field on EHD propulsion were tested. The thruster was tested in a B field one order of magnitude greater than the Earth field, oriented vertically along the axis of the thruster. This had no effect within the 10 µg accuracy of the measurements.

Around this same time, Wilson conducted a number of tests exploring various aspects of EHD thrusters for NASA [25]. The first tests sought to confirm Tajmar's results concerning the lack of a coupling between the electromagnetic and gravitational fields. Using a hexagonal "lifter", or six equilateral triangle lifters pieced together, it was shown that the entire thrust was due to electric wind. Furthermore, a "box lifter" using 13 parallel collector electrodes each paired with a wire emitter was tested in a horizontal orientation, showing an independence from gravitational interaction. A second test was conducted to study the effect of different emitters. Traditional lifters use wire emitters, whereas Christenson's thruster as well as some of Canning's designs used pins. Whereas a wire can only vary in its radius, pins can vary in their spacing as well as tip radius. Wilson's pin emitters consisted of a thin brass sheet with household pins soldered on in a line. In general, pin emitters performed better than wires including having a lower V_o, and a spacing of roughly 29 mm between pins was seen to be optimal. A further test was conducted with several pin emitters lined up parallel to each other. The emitters were spaced apart at four test distances, and the best performance was seen not at the longest or shortest separation, indicating some local optimum. Smaller tip radii showed higher performance, but the smallest tips with initial radius 2 µm showed erosion after several tests. The optimal design from these previous tests was then used in a study for the optimal gap length d. Tests

were conducted at five discrete distances ranging from 19 to 95 mm, and the highest performance was seen between the 57 and 70 mm gaps. In looking at $^{F}/_{P}$, it was noted that at higher thrust, the ratio collapsed together for the different gap lengths, but that at lower thrust values, they separated so that larger gaps had higher ratios.

Wilson, in order to obtain higher thrust values, also tested with larger thrusters. Two frames were constructed with lengths of 457 and 914 mm. The collectors were made of aluminum tubing, shaped in a crude airfoil shape with thickness-to-chord ratio of 0.5. Another test for the emitter was conducted, this time comparing a wire, pins, a series of razor blades, and a single razor-sharp emitter. The razor emitters showed less thrust than either the wire or pins, and again the pins were superior to the wire. The collector was then varied to study its effects. The general shape, including the thickness-to-chord ratio of 0.5, was maintained, but the length and frontal area were varied. Four sizes were tested, and the performance increased monotonically as the collector grew in size. In a followup, two collectors were used with a single emitter. Varying their spacing from 0 (single collector) to 44 mm, an optimum was found at 33 mm. However, Wilson noted that this may also depend on gap length, which was held constant throughout this test.

A final series of tests was conducted by Wilson to study pulsed excitation. Pulse durations as well as their frequency could be varied independently. First, a test was conducted with 10 µsec pulses of 20 kV on top of a 10 kV DC bias. The force was identical to the DC case at a frequency of 30 Hz, but then increased monotonically with frequency to 1 kHz. A test with 0 DC bias showed that the DC voltage was not contributing to the thrust beyond roughly 300 Hz. The pulse was then shortened to 1 µsec, which showed the same performance as before. However, the shorter pulse allowed for higher frequencies, and it was shown that above 5 kHz, the pulses performed much as a DC bias would, with an asymptote at the thrust level of a DC 20 kV thruster. Much shorter pulses, on the order of tens and hundreds of nanoseconds, showed lower levels of thrust.

In 2010, a team from the École Centrale Paris in France attempted to separate the processes of ionization and acceleration in order to maximize the power input to

the airflow [11]. Simulations in COMSOL MULTIPHYSICS allowed for the design of a wire-cylinder-plate configuration which would align the electric field parallel to the thrust vector. A single wire emitter formed an ionization zone with two grounded cylinders, and downstream plates were biased to best shape the field. A glass Pitot tube was used to measure velocity, and the thrust was calculated from the velocity profiles. Compared to a reference configuration consisting of just the wire and plates, a 46% increase in thrust was achieved for a 16% increase in power consumption. The gap sizes used in this study were 3 mm between the wire and cylinders, 4 mm between the cylinders and plates, and 8 mm between the two cylinders; effects for larger geometries are unknown.

Another team from Yonsei University in South Korea studied the effects of stacking multiple ionic wind generators [16]. Each generator consisted of a circular emitter electrode with multiple pins paired to a wider ring collector electrode further downstream. A hot-wire anemometer and vane anemometer were placed beyond the last stage to measure exit velocities. A study of the voltage-current relations for each individual generator showed approximately the same electrical characteristics for all stages. As such, if the same voltage is applied across each stage, the total current would simply be $I_{tot} = nI_1$ where I_1 is the current out of a single stage and n the number of active stages. As the number of active stages was increased, it was shown that both the flow velocity and energy efficiency increased with the square root of n.

Chapter 3

Experimental Setup and Procedures

This chapter will present the experimental setup for single-stage and dual-stage thrusters. For each case, the setup construction and electrical connections will be discussed, and the testing methodology will be explained. The experimental setup was designed so that both single- and dual-stage thrusters could be tested with minimal modification. The requirements for the EHD thruster experimental setup were:

1. Ensure user safety throughout the entire range of possible thruster operations,
2. Allow for thruster operation with minimal interference to electrical and aerodynamic properties,
3. Accurately measure the applied voltage, current, and thrust output,
4. Allow for rapid access to the thruster in order to modify geometry.

3.1 Single Stage Thrusters

One of the goals of this project was to confirm the single-stage data collected by Payton [20]. As such, the electrode configuration for this work was selected to use a

wire emitter so that the results would be comparable. However, as discussed below, the design was modified in order to counter issues learned in earlier experiments.

3.1.1 Construction

The main experimental setup consisted of two major components, the thruster and a load cell to accurately measure thrust. An electrohydrodynamic thruster consists of three parts: the emitter electrode, the air gap, and the collector electrode. From previous works as well as the thrust equation 1.17, it is known that the air gap has a significant effect on the thrust. As such, one major design consideration was to allow for numerous changes to the gap d. From traditional "lifter" designs, there are also several lessons to be learned. First, the triangular (or other polygonal) designs incorporate sharp corners, which do not conform to the one dimensional assumption in the theory development. Second, the aluminum foil often used for the collector is easily crumpled, leading to locally reduced radii of curvature and thus differing corona discharge properties. Summarizing, the key design considerations were:

1. Adjustable wire electrode to vary air gap d,
2. Robust construction for collector electrode to mitigate deformation,
3. Electrodes long relative to other characteristic lengths with no sharp corners.

Figure 3-1: Thruster frame

In order to account for all of these, a square frame as shown in figure 3-1 was designed. The term "thruster frame" will be adopted to refer to this structure. In order to keep the two electrodes from being electrically shorted, a non-conducting material was necessary for the frame. A square polytetrafluoroethylene (PTFE) Teflon rod 0.375×0.375 in. was procured, and three lengths each 40 cm were cut. The bottom side of the frame was the collector electrode, cut from aluminum 6061 tubing. The tube had an outer diameter of 0.25 in. and an inner diameter of 0.180 in. The collector was connected to the PTFE side beams using stainless steel sprig pins, which doubled as electrical leads to the ground or power supply. The PTFE rod opposite the aluminum collector was connected to the two side pieces using nylon eyebolt nuts.

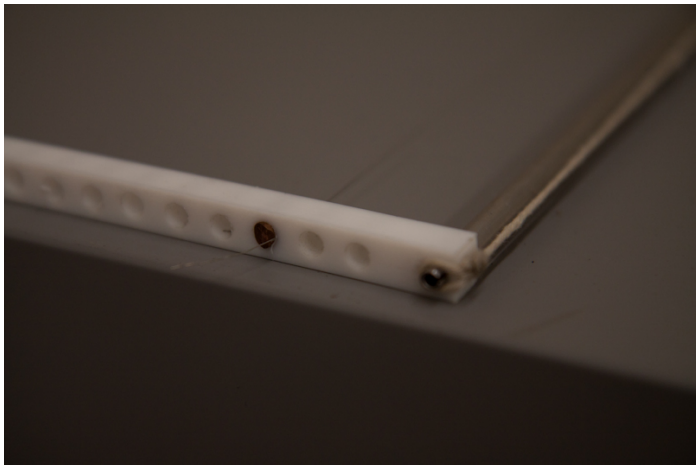

Figure 3-2: Single stage wire connection

Along the length of the two side pieces of the thruster frame, holes were drilled at 1 cm increments for the emitter electrode wire. The holes were drilled large enough so that a 4 American Wire Gauge (AWG) wire could be fit snugly. This was to allow for dual stage tests, to be described below. The first hole, corresponding to $d = 1$ cm, was placed so that the very bottom of the hole would be 1 cm away from the top of the collector electrode. The emitter wire was selected to be Solid Tinned Copper 35 Standard Wire Gauge (SWG), or 32 AWG, in accordance to Payton's design. 32 AWG wire has a diameter of 0.202 mm, much smaller than the 4 AWG wire with diameter 5.189 mm. In order to hold the emitter wire in place, two small pieces of 4 AWG wire (≈ 0.25 in. long) were cut to fit in the frame holes as stoppers. The

emitter wire was first placed in the hole, and the stoppers were slipped in from the inside of the frame so as to hold the emitter in the correct position at the bottom of the hole and apply tension on the emitter, as shown in figure 3-2.

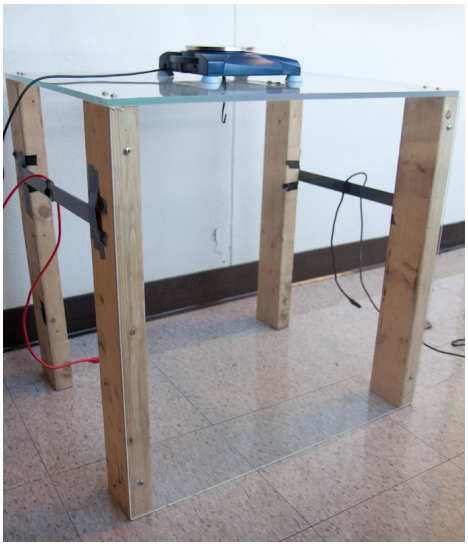

Figure 3-3: Load cell table

The other major component, henceforth referred to as the "table" (see figure 3-3), was designed to allow for accurate measurement of the thrust without interfering with thruster operation. The table size was dictated by a balance between fitting in the fume hood, as discussed below, and being large enough to not change the electric field. The legs were cut from wooden beams, each to 60 cm. The table top was an acrylic sheet $24 \times 20 \times 0.375$ in., treated with a static electricity dissipating coating. A 2 cm hole was drilled in the middle of this sheet so that the thruster could be connected to the Ohaus Scout Pro SP602 digital scale placed on top of the table. The SP602 has a built in hook connected to the pan so that the thruster could be hung underneath. This scale has a capacity of 600 g with precision to 0.01 g. A separate attachment allowed for connection to a computer via USB so that measurements could be recorded. Another acrylic sheet was placed on the front face of the table in order to protect the user. The other three sides were left open to allow for ventilation around the thruster, however thin PVC beams were attached horizontally on the two sides to act as anchors for the electrical leads between the

power supplies and thruster.

The thruster frame was hung from the digital scale's hook. As the hook itself did not extend low enough, an S-shaped hook was hung from the scale. The two eyebolt nuts were strung together with a cotton string, and the S-hook was connected to this. The entire weight of the thruster, $\approx$ 240 g for the single-stage thruster, was supported by the scale, and the thruster was oriented so that thrust would be seen as a reduction in weight. See 3-4 for the complete setup.

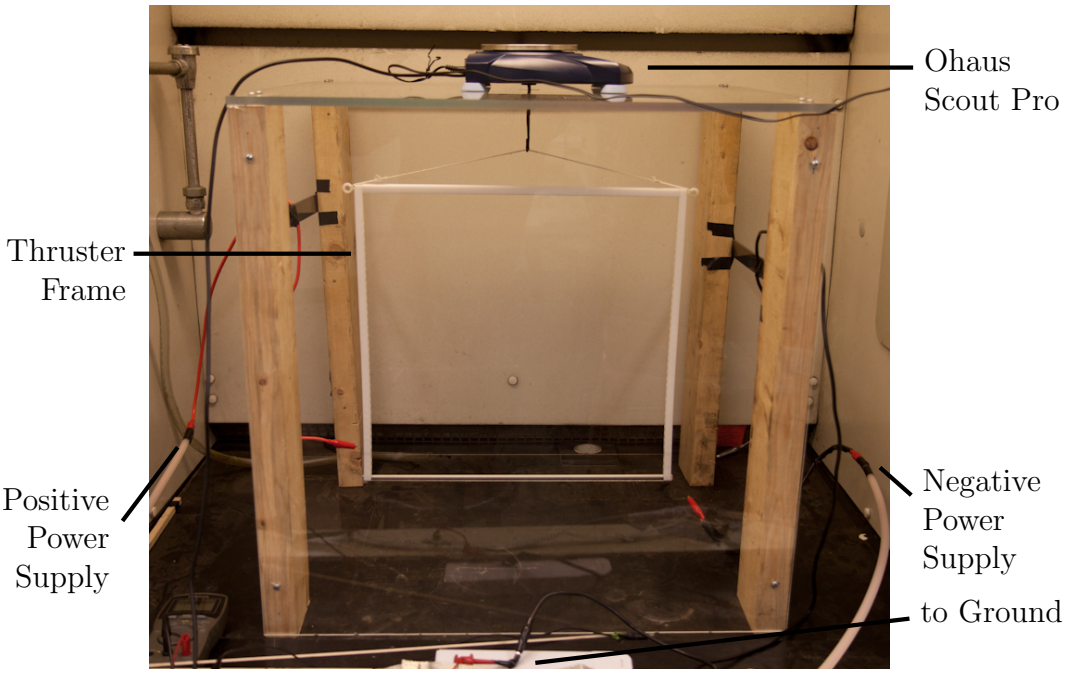

Figure 3-4: Complete experimental setup

3.1.2 Electrical Wiring

The experiments called for electrical power supplies providing a high enough voltage and current to ensure operation of the thruster without externally limiting the corona discharge. For the 40 cm thruster frame, a maximum gap of 21 cm was planned so that a 1:2 ratio between the gap and electrode length could be maintained in accordance to the one-dimensional assumption made in the theory derivation. Electrical breakdown in air occurs at approximately 10 kV/cm, which would allow for up to 210 kV to be applied to a $d = 21$ cm thruster. It was known from previous works

that lifters operating at tens of kilovolts require several tenths of milliamps. With these considerations, power supplies capable of supplying over 100 kV and 1 mA were selected. The Matsusada AU120P2.5 and Matsusada AU120N2.5 power supplies provided up to 120 kV and 2.5 mA in positive and negative polarities, respectively. The supplies also had over-current protection, important for when arcing occurred. A 10-turn potentiometer controlled the output voltage, and both voltage and current readings were provided by 3.5 digit meters accurate to within 1% of the max outputs. The power supplies were powered by standard 120 V sockets, and they were further grounded to a cold water pipe.

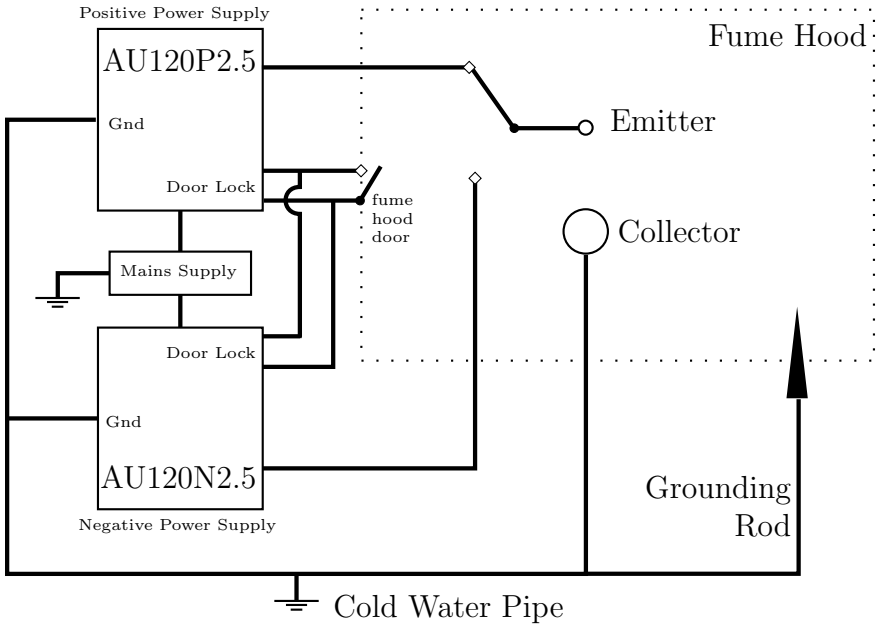

Figure 3-5: Single stage thruster circuit diagram

The power supplies were placed outside of the fume hood to allow access to the potentiometer. High voltage insulated cables fed power into the fume hood. These cables were also provided with ground ribbons, which were connected to the cold water pipe. 10 AWG insulated cables were connected to the power supply outputs, supported in place using the PVC beams on the table. These cables were provided with alligator clips so that they could connect to the thruster electrodes.

For single-stage thrusters, only one power supply was used at any one time. As such, the appropriate lead cable was connected to the emitter wire. The collector was

grounded via the sprig pins to the ribbons on the high voltage cable. The wiring for both connections were made so that they did not apply a force on the thruster frame.

3.1.3 Experimental Procedures

Single-stage thrusters were tested for a range of gap lengths and with both polarities. At the beginning of each trial, the thruster was fitted with the emitter at the appropriate gap d. Before hanging the thruster, the digital scale was calibrated to zero. The cotton string was used to hang the thruster in the table and adjusted so that the thruster was angled properly, with the collector parallel to the tabletop and fume hood floor. The cable from the appropriate power supply was connected to the emitter, and the grounding wire was attached to the collector.

Before the main experiments, several trials were conducted in order to observe any hysteresis. A pretrial was conducted to determine the upper voltage threshold before arcing. Then, after allowing time for ventilation and for the power supply to return to zero voltage, the voltage was raised in 1 kV increments. Upon reaching the maximum voltage, selected as the maximum integral value at least 1 kV below the arcing voltage, the applied voltage was decreased at the same increment to zero. After each voltage change, a few seconds were allowed for the electrohydrodynamics to stabilize in its new operating point. The timescale for this stabilization can be estimated from the drift time of ions in the gap:

$$t = \frac{d}{v_D} = \frac{d}{\mu E} = \frac{d^2}{\mu V}. \tag{3.1}$$

The maximum time is given for the weakest electric field, so using a voltage of 1 kV, a gap of 20 cm, and the ion mobility in air of 0.0002 m^2/sV as reported by Tyndall [24],

$$t = \frac{.2^2}{.0002 * 1000} = 0.2 \text{ s}. \tag{3.2}$$

Therefore, a few seconds were sufficient for performance saturation. Figure 3-6 shows the results from a hysteresis trials with $d = 1$ cm. The voltage-current relationship

shows no significant deviation between the voltage increase (up-run) and decrease (down-run) phases. However, the thrust values on the voltage decrease phase show greater values by as much as 5 mN, with a nonzero "thrust" reading at zero voltage. The inflated values on the down-runs are partially attributed to the presence of species ionized by the higher voltages at previous measurement points. The larger voltage ionized a larger number of molecules, and some of these did not get accelerated directly towards the collector, but rather along a farther out path. The current measurement is taken in series with the emitter, so their ionization would have been accounted for at the higher voltage step, but their persistence into the lower voltage steps may have increased the observed thrust. This effect would not be seen in the up-runs, as confirmed by repeated tests shown in figure A-1. The observed difference at zero voltage cannot be explained by the persistence of ions; however there may have been an issue with saturation on the digital scale, as tests with known weights showed lingering readings on the order of 0.1 to 0.2 g after all weights were removed. Given the demonstrated repeatability in the up-run phases, it was decided satisfactory to proceed with recalibration before each experiment and proper ventilation time between all trials.

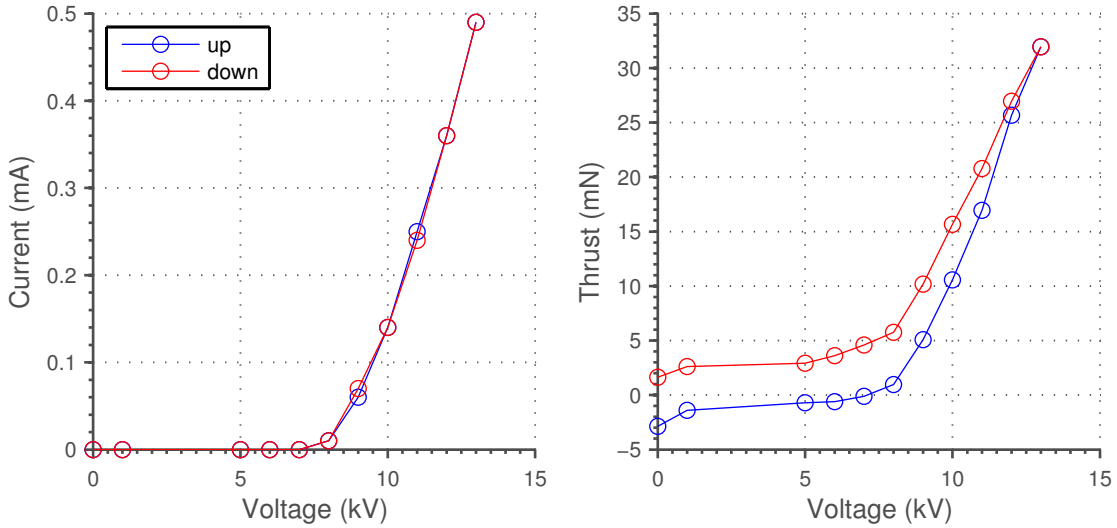

Figure 3-6: Hysteresis for $d = 1$ cm single stage thruster

The main experiments were conducted similarly but without the decreasing volt-

d (cm)	1	2	3	4	5	7	9	11	13	15	18	21
$+V_{max}$ (kV)	13	20	29	34	39	45	53	58	64	68	70	74
$-V_{max}$ (kV)	12	20	29	34	39	45	53	58	64	68	68	n/a

Table 3.1: Gap lengths and maximum voltages

age. For each trial, a value of d was selected and the thruster mounted in the table. After recording the initial weight so as to have a basis for calculating thrust, the applied voltage was increased in 1 kV increments up to the maximum integer voltage before arcing. At each increment, the voltage, current, and weight were recorded. After testing to the maximum voltage, the power supplies were shut down and the thruster manually grounded using the grounding rod described in section 3.3. Each configuration, including both geometry and polarity, was tested two or three times to demonstrate repeatability.

In order to test a wide range of single-stage thruster configurations, a number of gap lengths were tested. The values of d are summarized in table 3.1 along with the maximum tested voltages. For each gap length, both positive and negative polarities were tested.

The 21 cm test could not be completed for the negative polarity as the insulation on the cables failed and arcing occurred between the lead cable and fume hood surfaces.

3.2 Dual Stage Thrusters

The experiment was designed to allow for dual stage tests to be conducted with minimal modifications to the frame and table.

3.2.1 Construction

The dual stage thruster introduced an intermediate electrode in between the emitter and collector. In order to maintain similar corona properties to the single stage for $d_1 = d$, where d_1 is the first gap in the dual stage and d is the single stage gap, the intermediate electrode was selected to have a similar radius to the collector. Wires,

as discussed above, come in standard sizes dictated by the American or Standard wire gauges. The intermediate electrode was sized to be no larger than the collector so that while maintaining the electrical properties, it would not impose too large of a surface area blocking the current to the collector, thereby reducing ψ. 2 AWG wire was thus too large, and 3 AWG with diameter 5.827 mm was just smaller than the aluminum tube. However, due to commercial availability, a single strand 4 AWG wire with diameter 5.189 mm was selected. Due to the thickness of the wire, it could be treated as rigid and had to be straightened.

Once the gaps d_1 and d_2 were known for each trial, the 4 AWG wire would be attached to the frame using the appropriate holes. The emitter wire was then connected as in the single stage case, but instead of being placed at the very bottom of the hole, the wire was placed at the very top of the hole as shown in figure 3-7. This ensured that the air gap from the emitter to the closest point on the intermediate electrode was equal to the desired value of d_1, and the shortest distance between the collector and intermediate electrode was equal to d_2.

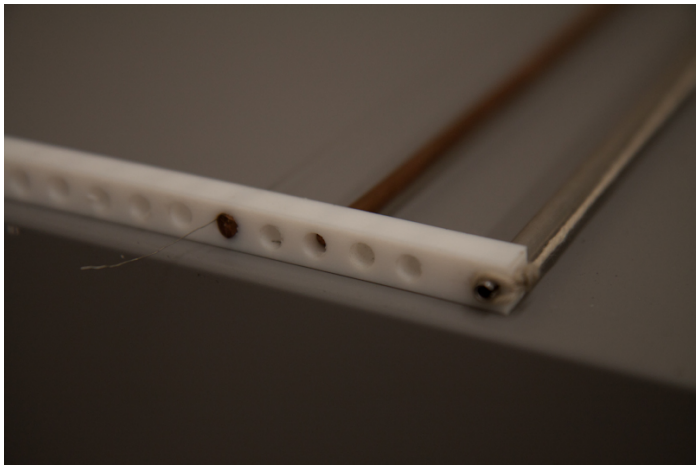

Figure 3-7: Dual stage wire connection

Another series of tests was conducted with an insulated intermediate electrode. This was done so as to adhere better to the ideal performance in which no current flows in or out of the intermediate electrode. For these tests, a 10 AWG insulated wire was used as it had a similar radius to the 4 AWG bare wire. The insulated wire was connected to the frame in an identical manner to the bare electrode.

The table did not need any modifications to be used for the dual stage tests. The weight of the thruster with the intermediate electrode was ≈ 320 g, within the 600 g capacity of the Ohaus Scout Pro.

3.2.2 Electrical Wiring

In order to create the two voltages V_1 and V_2, both Matsusada power supplies were used for every dual stage test. The emitter was connected to the positive polarity supply, and the collector to the negative polarity supply. The intermediate electrode was grounded. A lead ≈ 5 cm long connecting the intermediate electrode to the alligator clip on the ground wire was made with the 32 AWG wire so that this connection did not apply any external forces on the frame. This electrical layout ensured the highest potential at the emitter and the lowest at the collector. As potential differences as high as 30 kV would exist between the two power supply cables, the electrical leads were placed at opposite ends of the fume hood.

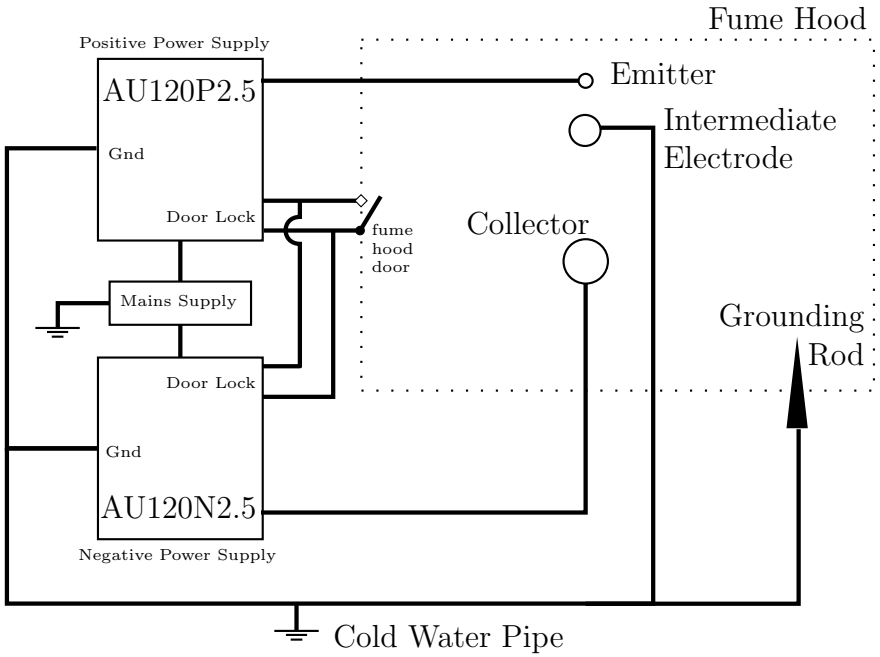

Figure 3-8: Dual stage thruster circuit diagram

The voltages and currents applied by each power supply were read from the digital meters. An ammeter was connected in series with the grounding wire between the

intermediate electrode and the grounding ribbon.

3.2.3 Experimental Procedures

Dual-stage thrusters were tested for a variety of gap lengths so as to be able to observe several relations. The effect of varying the gap lengths and voltages were studied, and more importantly they were compared to single-stage thrusters. A single dual stage design could be compared to two single stage cases: $d_1 = d$ and $d_1 + d_2 = d$. The first case tests for any advantages of a dual stage design given the same electrical requirements, and the second case tests for any advantages of a dual stage design for the same volumetric requirements.

In order to have enough points for comparison, the following gap lengths were tested: $d_1 = \{1, 2\}$ cm and $d_2 = \{3, 4, 6, 13\}$ cm. Every combination of the two gaps were tested. With the gap lengths set, V_2 was set to one of three constants, $V_2 = \{5, 10, 20\}$ kV. For each value of V_2, the independent variable V_1 was increased in 1 kV increments up to the maximum voltage before arcing. At each increment, the voltage applied by each power supply, the current through all three electrodes, and the weight were recorded. After shutting down and manually grounding all electrodes, each configuration was rerun in order to test for repeatability.

This set of parameters allowed for observations of the following:

1. Effect of varying V_2 for the same geometry,

2. Effect of ratio $^{d_2}/_{d_1}$ for the same total gap length,

3. Effect of varying d_2 for the same d_1,

4. Comparison of single stage thrusters to dual stage thrusters with $d = d_1$,

5. Comparison of single stage thrusters to dual stage thrusters of the same total gap ($d_{tot} = \{4, 5, 7, 15\}$ cm) .

3.3 Safety Considerations

Several steps were taken in order to ensure the user's safety while conducting experiments. The table and thruster were placed inside of a fume hood, which allowed for safety measures against all expected risks.

EHD thrusters operate at high voltages, often at tens of kilovolts. At these voltages, arcs may span several centimeters, carrying enough power to endanger the user's life. The first layer of protection was the front facing acrylic sheet, as mentioned in the construction section. A second layer of protection was the fume hood, which had a sliding door to restrict access. A microswitch in series with the power supplies' door lock was placed in the fume hood so that the output would only activate with the screen door closed. A release of the microswitch would immediately cut off all current out of the power supplies. A final layer of protection was a conductive wire mesh attached to the outside of the fume hood, in front of the screen door. This mesh was grounded to the experimental common ground and functioned as a Faraday cage to capture high energy particles.

Before any physical contact with the thruster after an experimental trial, a manual earthing probe was used in order to ensure full discharge of all electrodes. The probe was constructed as a wooden rod with a metallic tip grounded to the cold water pipe.

Aside from the hazards involving electrical discharge, the experimental design required protection from ozone inhalation. Ozone is an irritant and can be toxic at higher concentrations. Operation of the thruster inside the enclosed fume hood ensured proper ventilation.

The use of the fume hood as a housing for the experimental setup satisfactorily shielded the user from all expected risks. Three layers of protection prevented any electrical arc beyond the working area in the table load cell, and the fume hood flow vented all byproducts, including ozone and persisting ionized species.

Chapter 4

Results

Data was collected for various single stage and dual stage configurations as described in the previous chapter. Repeat trials for each configuration showed good agreement to each other, as shown in figure A-1 which has a mean standard deviation of 0.3162 mN. As such, the data presented here will be averaged data from all trials run for any particular configuration. It is known that corona discharge properties and ion mobilities are susceptible to variation with atmospheric conditions including pressure, temperature, and humidity. However, trials run throughout different weather or times of day did not show variations greater than the level of noise observed between trials conducted under the same conditions otherwise. Adding the trials under different external conditions to the data in figure A-1 decreased the mean standard deviation to 0.2582 mN. The convention for all plots in this section will be open circle data points for single-stage thruster data and closed data points for dual-stage thruster data.

4.1 Single Stage Thrusters

The single stage thruster was 40 cm long, consisting of a wire emitter ($\varnothing$0.202 mm) and an Aluminum tube collector ($\varnothing$6.35 mm). The gap d was variable in 1 cm increments. A positive or negative polarity high voltage was applied to the emitter via a Matsusada power supply, while the collector was grounded. The positive and neg-

ative polarities behaved similarly, and the positive polarity results will be discussed. Comparisons to the negative polarity case will be made in section 4.1.2.

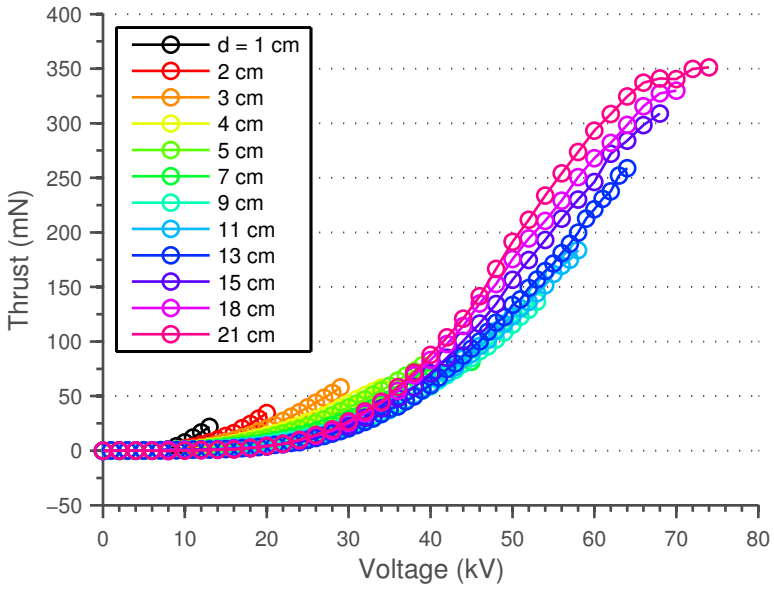

Figure 4-1: Voltage-thrust relationship for varying air gap, positive polarity

Figure 4-1 shows the voltage-thrust relationship for positive polarity voltages applied on EHD thrusters with varying air gaps. As predicted, no thrust is seen at lower voltages below the critical threshold corona inception voltage, but beyond that the thrust increases quadratically. As seen in equation 1.21, F is predicted by empirical relationships to vary with the product $\frac{V(V-V_o)}{d}$. The presence of the gap length d term in the denominator suggests that for a given voltage, a smaller gap results in a larger force. The data does show this trend for gaps up to $d = 9$ cm. Although able to generate higher forces at lower voltages, smaller gaps are limited in their maximum thrust output by the earlier onset of electrical breakdown and arcing, beyond which no thrust is produced. At gap lengths beyond 9 cm, the trend reverses and higher thrust is seen for a given voltage as the gap increases. This behavior is not predicted by the one dimensional theory, and one possible explanation is the deviation of the thruster geometry from the assumption that the electrode length is much larger than the gap length, $L \gg d$. Further tests are necessary with larger setups to determine how far this trend continues. If the geometric requirements for a thruster allow for

design in this range, then larger gaps will become preferable for producing higher thrust at a given voltage. Considering the higher $^{F}/_{P}$ values at larger gap lengths as discussed below, as well as the higher thrust limit as a function of the arc onset, this design range offers a larger range of thrust with a reduced electrical power input requirement.

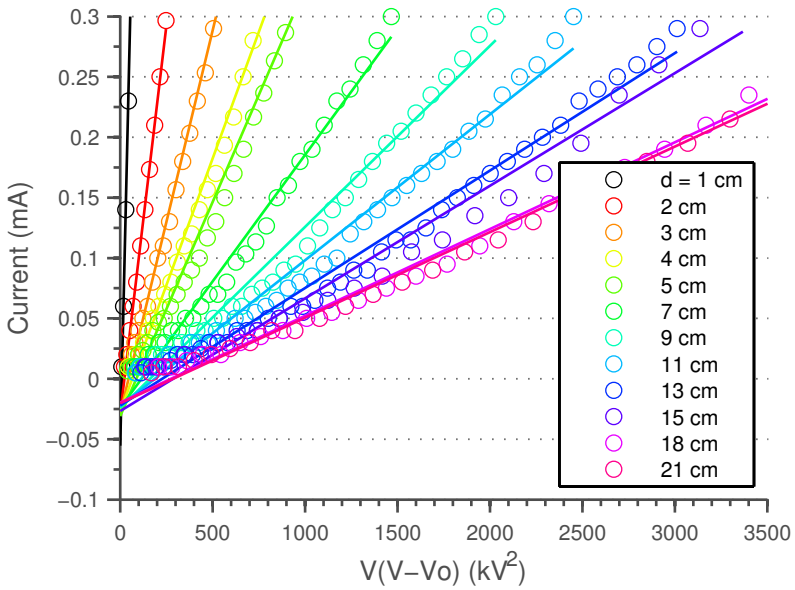

Figure 4-2: Voltage-current relationship for positive polarity

The current, given by equation 1.18, is predicted to vary linearly with the product $V(V-V_o)$. Figure 4-2 shows that a linear fit does approximate the relationship. Also, larger gaps are seen to allow less current to flow for a given applied voltage. This fits the empirical model by Cooperman [12], and makes sense as a larger air gap will result in a larger impedance. Finding the intersection of this plot with the horizontal axis allows for an approximation of the corona inception voltage V_o, included in table A.1. At larger gaps, a slight change in the slope can be seen at higher currents. This corresponds to the "bilinear effect," which will be studied in section 4.1.1. Equation 1.17 predicts a linear relationship between current and thrust, and thus F is also expected to vary linearly with $V(V-V_o)$. This is shown in figure A-2 for a subset of the gap lengths; larger gap lengths were omitted for clarity. The change in slope due to the bilinear effect is visible in this relation as well.

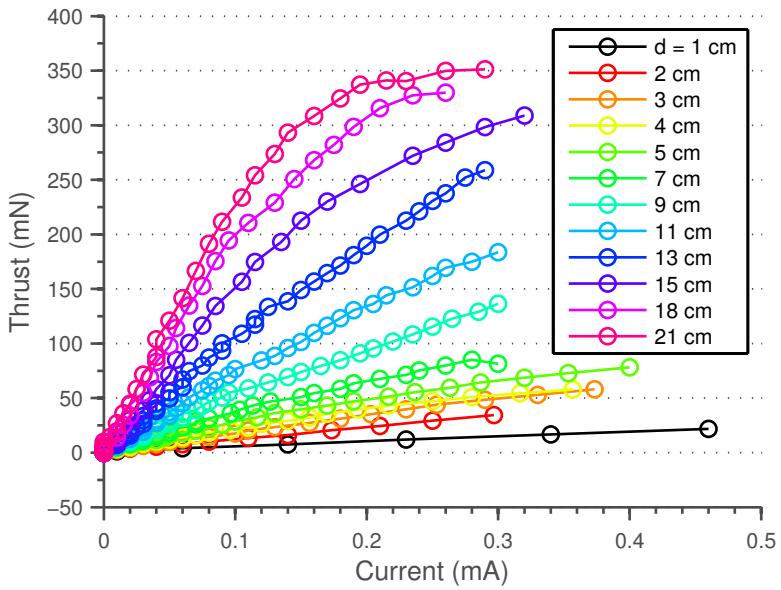

Figure 4-3: Current-thrust relationship for positive polarity

As predicted by theory, the data shown in figure 4-3 shows that for a given current, larger gaps produce larger thrusts. However, the linear relationship predicted by equation 1.17 does not hold beyond some threshold due to the bilinear effect. For gaps under $d = 15$ cm, the thrust varies in two linear regimes, with the regime at higher currents showing a decreased slope. At the larger gaps beyond $d = 15$ cm, there is a nonlinear decay in performance. The bilinear effect, studied more extensively in section 4.1.1, does not predict this nonlinear decay. One possible explanation is the deviation from the assumption $L \gg d$.

By using the current output data and the ion mobility values given by Tyndall, the electrohydrodynamic thrust can be compared to theoretical predictions. The ion mobility values for dry and saturated air are given as $\mu_{dry} = 2.155 \times 10^{-4}$ and $\mu_{sat} = 1.598 \times 10^{-4}$ m^2/Vs [24]. Figure 4-4 shows the comparison for the $d = 3$ cm case.

The two predictive lines are approximations of the maximum and minimum expected forces for a given current, as the real ion mobility is expected to fall in between the dry and saturated cases. The exact values by Tyndall correspond specifically to the temperature and pressure at the time of their experiments, but the effects of the

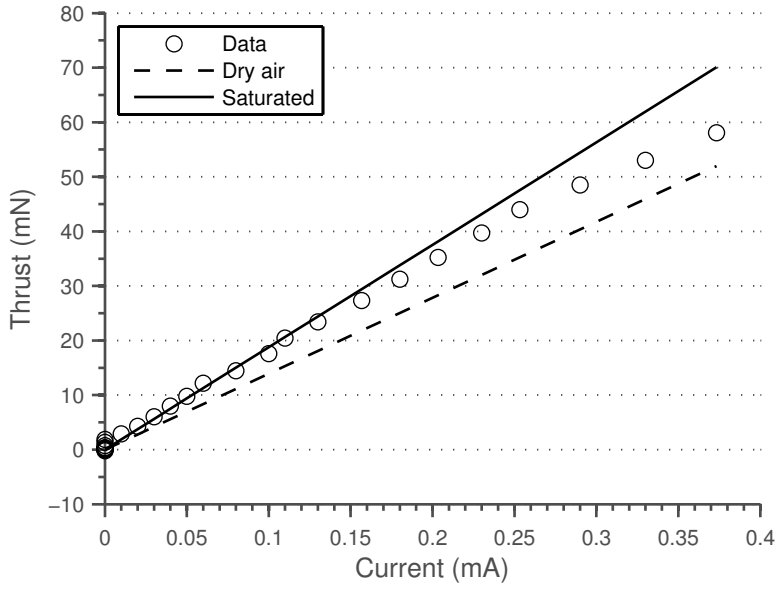

Figure 4-4: Comparison to theoretical prediction for $d = 3$ cm

pressure and temperature variation within the fume hood are included in the variation observed between repeat trials, and thus the lines are treated as accurate estimates of the bounds. The experimental data fits well within the expected bounds, and the same is observed for all gaps up to $d = 11$ cm. Beyond this gap, as shown in figure A-3, the experimental data outperforms the theoretical bounds, generating higher thrust at a given current than predicted. Given the similar threshold gap length, this effect may be related to the reversal of trends seen in the voltage-thrust relationship shown in figure 4-1.

The thrust-to-power ratio is predicted to increase with gap length for a given voltage. Figure 4-5 confirms this, as larger gaps are shown to consistently have larger $^{F}/_{P}$. As seen by the presence of voltage in the denominator of equation 1.27, the ratio decreases as voltage, and thus thrust, is raised. Smaller thrust values are more susceptible to larger error due to the limited resolution of the measurement devices, and thus the initial value of the thrust-to-power ratio is obtained as a linear fit to multiple data points. Plotting the thrust vs power, as in figure 4-6, and fitting a line to all points below $P = 1$ W, gives a more robust number. The slopes, corresponding to the $^{F}/_{P}$ ratio for the points below 1 W in units of mN/W, are included in table

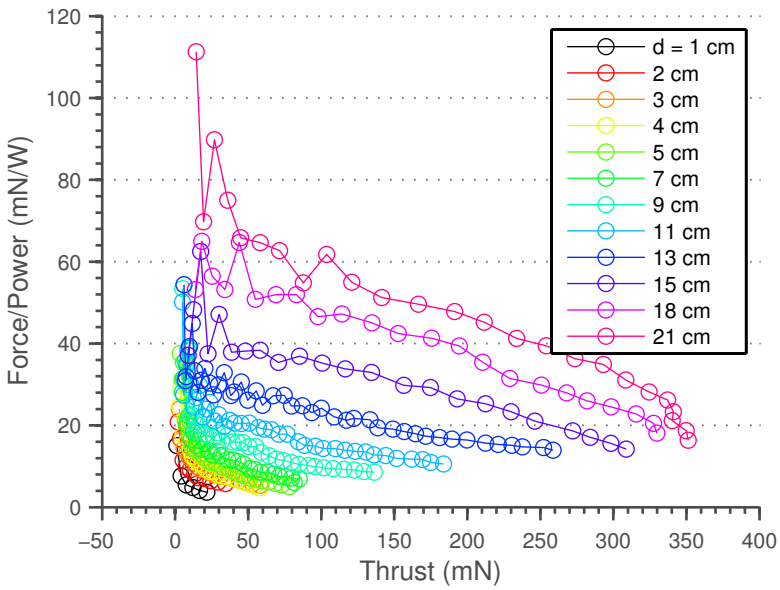

Figure 4-5: Variation in thrust/power as a function of thrust

A.1 for both positive and negative polarity cases. As predicted by theory, the value increases monotonically with gap length with a maximum value of 68.43 mN/W for $d = 21$ cm.

Comparing to Payton's numbers, the variation in $^{F}/_{P}$ with gap length is subdued. At $d = 1$ cm, the frame thruster generated 7.78 mN/W compared to Payton's 4.71 mN/W. However, by $d = 5$ cm, the numbers were 16.04 mN/W for the frame and 20.0 mN/W for Payton. A similar trend was seen for the corona inception voltage, which were observed at 6.92 kV and 11.14 kV for $d = 1$ and 5 cm, respectively, for the frame compared to 6.9 kV and 13.7 kV for Payton. Despite these different magnitudes, the directionality of all trends observed matched Payton's results, with the exception of the trend reversal in the voltage-thrust characteristic. Payton's maximum gap length was 6 cm, not large enough to have observed the effect. The differences in numbers can be explained by the contrasting geometry; the frame thruster was linear whereas Payton employed the triangular lifter geometry.

From a design perspective, a characterization of the current, voltage, and power required to generate a certain amount of thrust is necessary. These results are shown in figure 4-7 for a thrust of $F = 10$ mN. The plot on the left shows the required

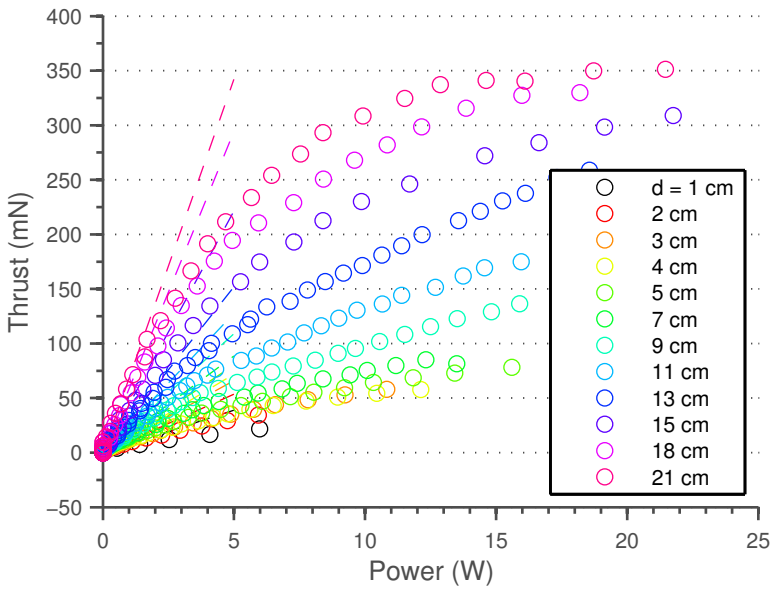

Figure 4-6: Thrust vs power for single stage thrusters, positive polarity

current and voltage as a function of the gap length. For a given force, assuming that the ion mobility μ is constant, the current I and gap length d are expected to be inversely proportional from equation 1.17. The current plot in black supports this inverse relationship. The voltage plot in red, as discussed above for the voltage-thrust relationship, shows a peak at $d = 13$ cm. The initial slopes just beyond the corona inception voltage in figure 4-1 decrease at larger gap lengths due to the smaller output current increments per applied kilovolt and the corresponding smaller thrust increments. The previously mentioned peak at 9 cm then becomes true for higher thrust values. The plot on the right shows the required power to generate the same 10 mN of thrust. This also shows an inverse relationship with gap length. The power reading of 0 W for $d = 21$ cm is due to the current output being less than the 0.01 mA resolution of the power supply ammeter. In considering the necessity of power generation for any practical use of EHD thrusters, this relationship shows that larger gap lengths require less power to generate a given thrust, but that there is diminishing return as the gap is enlarged.

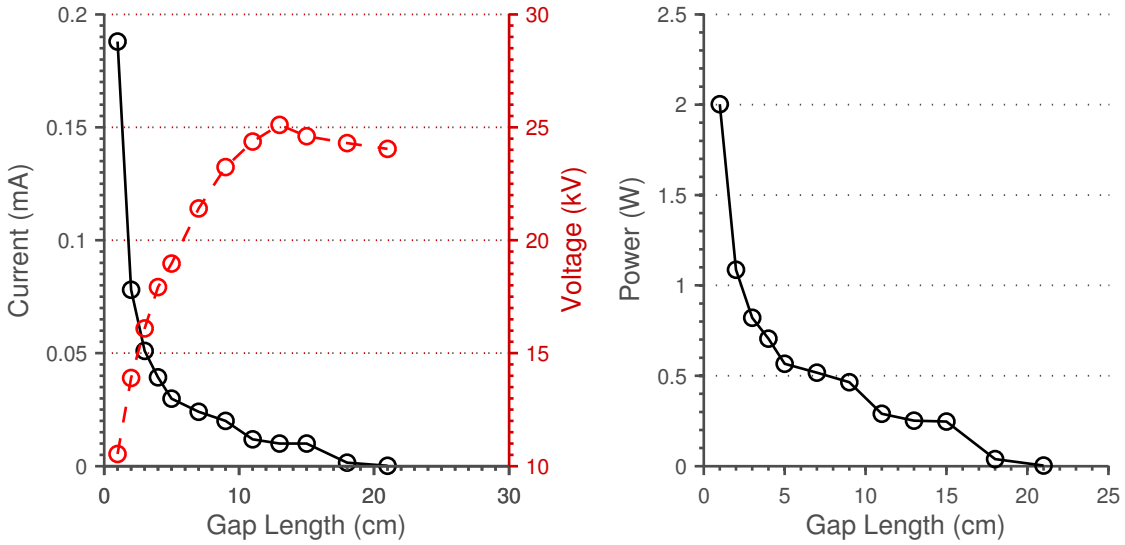

Figure 4-7: Current, voltage, and power draw for $F = 10$ mN

4.1.1 Bilinear Theory Results

The bilinear thrust variation with current is seen in figure 4-3, where for most curves, there is an initial linear variation and then beyond some threshold, a second linear regime with reduced slope. A theoretical model to explain this behavior was presented in section 1.3.1. Due to the limitation of the corona inception voltage models to specific geometries, the value of this secondary corona inception was not predicted from theory. The threshold was instead selected from the plot as a secondary inception current I_{o2} and perturbed so that the residuals for the two linear fits could be minimized. The selected thresholds and the corresponding secondary corona inception voltages V_{o2} are included in table A.1. Also included are the two slopes for each current-thrust relationship, labeled as a_1 and a_2.

The left plot of figure 4-8 shows the two linear fits for each geometry. The slope values a_1 and a_2, in units of mN/mA, correspond to the amount of additional thrust generated for a unit increase in the current output. All linear fits for both the initial and second regimes, except in the cases of $d \geq 15$ cm, have coefficients of determination (R^2) greater than 0.98. The gap values greater than 15 cm show a nonlinear decay in performance, causing the bilinear model to have a less accurate fit than for smaller gaps.

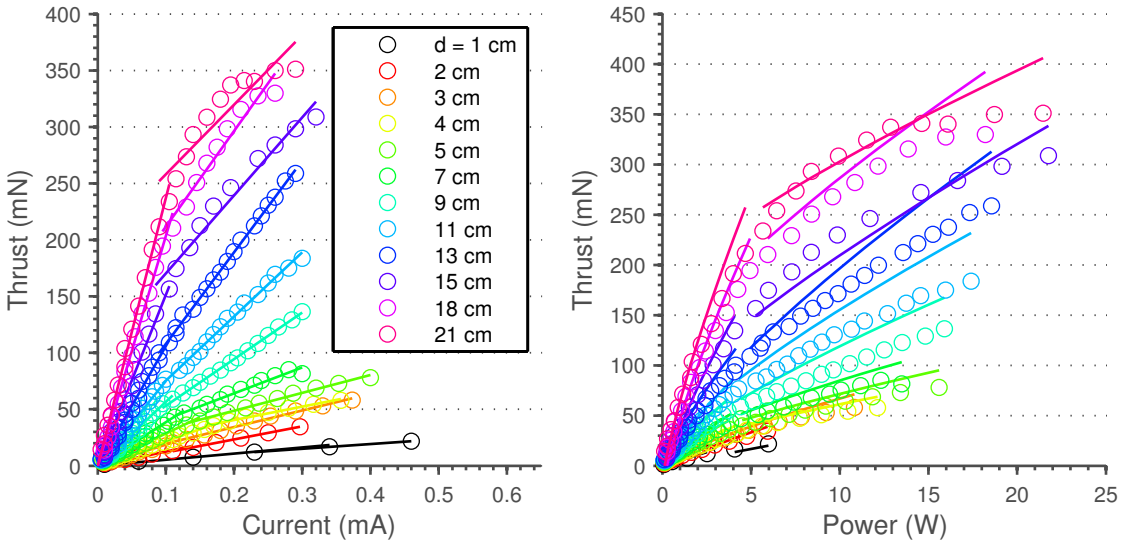

Figure 4-8: Left: bilinear fit for thrust-current relationship, Right: bilinear prediction for thrust-power relationship

The data is compared to the bilinear model in the right plot. The $^{F}/_{P}$ values were calculated using the values of a_1 and a_2 and integrated over power. These predictions are shown by the lines, and the open dots are the measured data. The gap in the two segments of predictions is an artifact of the use of empirical values for power. The bilinear model predicts a piecewise decrease in performance beyond the onset of the reverse current, greater than the decrease predicted by the presence of the voltage term in the denominator of the one dimensional model equation 1.27. The measured data demonstrates this degradation in performance, and in most cases the actual losses are greater than the predictions. The initial regime is fit more accurately by the prediction, and the location of the sharp degradation in the power-thrust relationship agrees with the bilinear model. The causes of the further losses in the second regime are unknown and require further study.

The relationship of the bilinear effect to the shifting slope in the I vs $V(V-V_o)$ plot was demonstrated in experiments with a lifter configuration, discussed in Appendix C. The point corresponding to the bilinear performance shift given by I_{o2} was plotted on a curve showing the voltage-current relationship in figure C-5, and matched well with the point where the slope shifts.

4.1.2 Negative Polarity Results

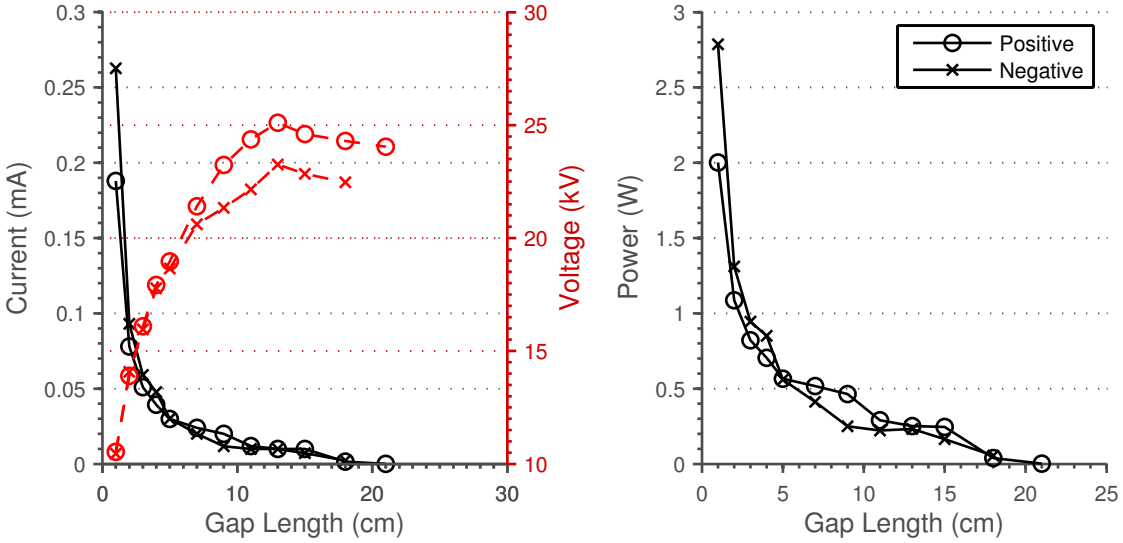

Figure 4-9: Required current, voltage, and power for $F = 10$ mN with positive and negative polarities

Negative polarity excitation for a single stage thruster showed performance similar to the positive polarity. All of the trends observed in the positive case, as discussed above, held true in the negative polarity data as well. Figure 4-9 shows the required current, voltage, and power for generating 10 mN of thrust for both positive and negative polarity excitations. At $d = 1$ cm, the negative polarity thruster requires over 0.07 mA more current, but for all other gap lengths, the difference between the two polarities is less than 0.02 mA. The voltage required is almost identical up to $d = 7$ cm, and at larger gaps is between 2 and 2.5 kV less for the negative case. Correspondingly, the only gap length for which the power requirement is significantly different is $d = 1$ cm, at which the negative polarity requires 0.8 W more power. At all other gap lengths, the difference is less than 0.3 W.

The voltage-current, voltage-thrust, and current-thrust relations are given in Appendix A. The negative corona output a higher current for a given voltage, with standard deviations ranging from 0.007 to 0.016 mA for gaps $d = 1$ to 5 cm. The negative voltage generates more force per volt, with a mean standard deviation as high as 1.403 mN over the domain for the $d = 5$ cm case. However, due to the higher

current also generated at the voltage, the thrust-power relation ends up very similar as shown in the right plot of figure 4-9. The similar abilities of the two polarities to convert electrical power into thrust is also seen in the $\frac{F}{P}_o$ values in table A.1.

4.2 Dual Stage Thrusters

The dual stage thruster added an intermediate electrode (⌀5.189 mm) to the single stage thruster. Both gaps, d_1 between the emitter and intermediate electrode and d_2 between the intermediate and collector, were variable in 1 cm increments. The emitter was raised to a positive voltage, and the collector to a negative voltage.

As discussed in the experimental procedures, dual-stage thrusters can be compared to the single-stage cases for two different sets of requirements, electrical or volumetric. In looking at maintaining a similar electrical performance, the cases where $d = d_1$ are studied. Total voltage requirements $V_{total} = V_1 + V_2$ will be compared to the single-stage V.

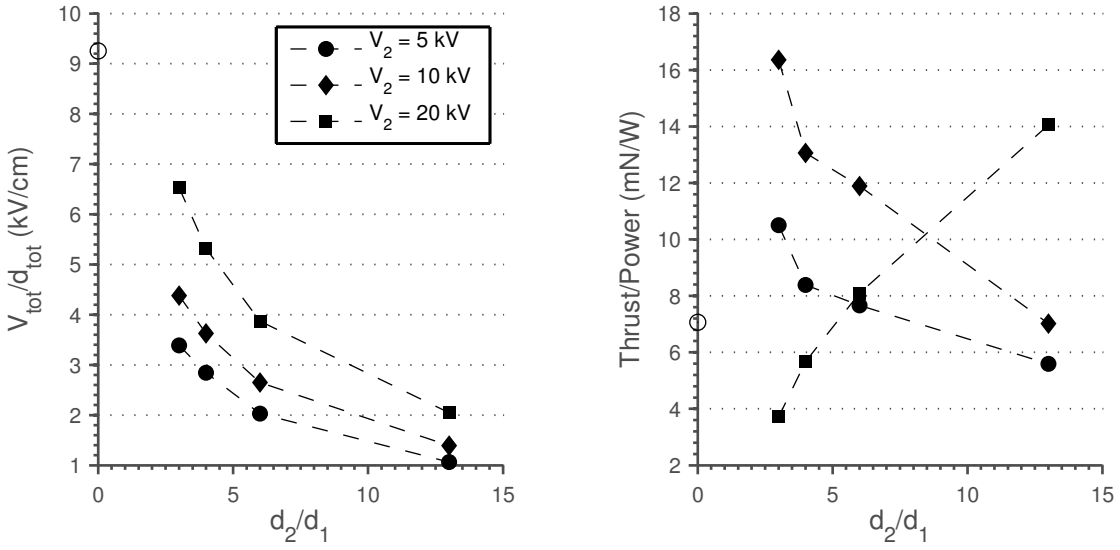

Figure 4-10: Variation of $^{V}/_{d}$ and $^{F}/_{P}$ with $^{d_2}/_{d_1}$ for $F = 5$ mN, $d_1 = 1$ cm

In order to generate equal thrust, in the case of figure 4-10 equal to 5 mN for thrusters with gap $d_1 = 1$ cm, the total electric field $E = ^{V_{total}}/_{d_{total}}$ decreases as the second gap is increased in length. This is possible without offsetting the corona incep-

tion due to the locally high field in between the emitter and intermediate electrodes. The same trend is seen for all three tested values of V_2, although higher values of V_2 created a larger average field. All dual-stage cases required a smaller average field strength than the 9.2 kV/cm single-stage case, shown by the open circle at ${}^{d_2}/_{d_1} = 0$.

The right plot of figure 4-10 shows the variation of the thrust-to-power ratio as the second gap is increased. For the cases of $V_2 = 5$ or 10 kV, as d_2 increases the ratio monotonically decreases. The thrust-to-power ratio for the smallest tested d_2 of 3 cm is improved at over 10 mN/W for $V_2 = 5$ kV and over 16 mN/W for 10 kV compared to about 7 mN/W for the single stage case with $d = 1$ cm. However, as the second gap is increased to the maximum tested value of 13 cm, the 5 kV case has a ${}^{F}/_{P}$ value under 6 mN/W, and the 10 kV case is even with the single stage at 7 mN/W. When V_2 is increased to 20 kV, the trend shifts to an upward trend. The thrust-to-power for $d_2 = 3$ and 4 cm are lower than the single-stage case, but as the gap increases the ratio increases as well, with a value over 14 mN/W at the maximum tested length. This reversal in trend for higher V_2 is likely the result of changes in the current distribution, as measured by the factor ψ. From the results of studying ψ, it is observed that the $V_2 = 20$ kV case has a higher proportion of the current flowing through the second gap, and thus is better able to take advantage of the increased gap length. However, at the lower values of d_2, the gain in performance from the increased gap is negated by the additional power consumption due to the second power supply, especially as a larger proportion of the current flows through the collector as opposed to the grounded intermediate electrode.

In order to assess the accuracy of the theoretical model given by equation 1.28, the case of a constant V_1 is studied as opposed to the constant F as above. Figure 4-11 shows the case for $d_1 = 1$ cm, $V_1 = 8$ kV, and $\psi = 0.5$. The value for ψ was set constant for the models, but in the experimental data varied from 0.3 to 1, as discussed in section 4.2.1. The theoretical predictions are shown by the lines, and if the selected value of ψ is decreased to zero, the y-intercept approaches the single-stage value and the slope of the line goes to zero. The empirical data for the case of $V_2 = 5$ kV has a negative slope as the second gap increases, indicating that it is not

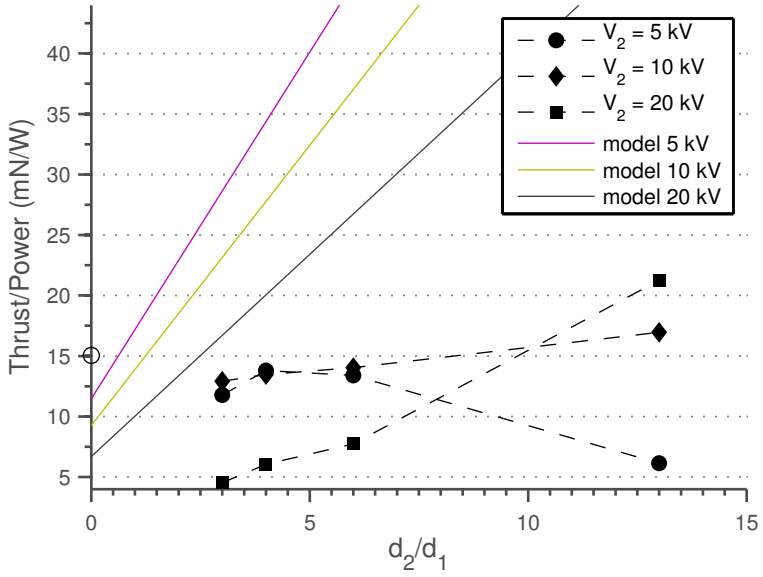

Figure 4-11: Comparison of $^{F}/_{P}$ to theory for $d_1 = 1$ cm, $V_1 = 8$ kV, $\psi = 0.5$

behaving as expected of a dual-stage thruster. $V_2 = 10$ kV has a small positive slope, indicating a small fraction of the current continuing into the second gap. This agrees with the ψ values between 0 and 0.09 seen for this configuration in section 4.2.1. V_2 = 20 kV has the highest slope, and is nearly parallel to the model prediction for $\psi = 0.5$. However, the actual values are displaced downwards from the predictions, indicating significant losses, possibly in cosine losses with the horizontal components of the electric field as well as collisions with the intermediate electrode.

In the case of comparing single-stage and dual-stage thrusters under a similar volumetric limitation, the cases of $d = d_1 + d_2$ are studied. The three plots of figure 4-12 do this for $d = d_{tot} = 4$ cm, with the first gap in the dual-stage cases $d_1 = 1$ cm. In the voltage-current relationship of the left plot, curves to the left indicate better effectiveness of the applied voltage at pulling current. As V_2 is reduced, the curve shifts left and approaches the single-stage case of $d = 1$ cm, equal to the first gap. This shift in the ability of the electrodes to pull current despite using the same geometry is attributed to the reshaping of the electric field due to the different voltages at the electrodes. Because of the higher current output, cases with lower V_2 require less total voltage to create a given thrust, as shown in the center plot. The case of $V_2 =$

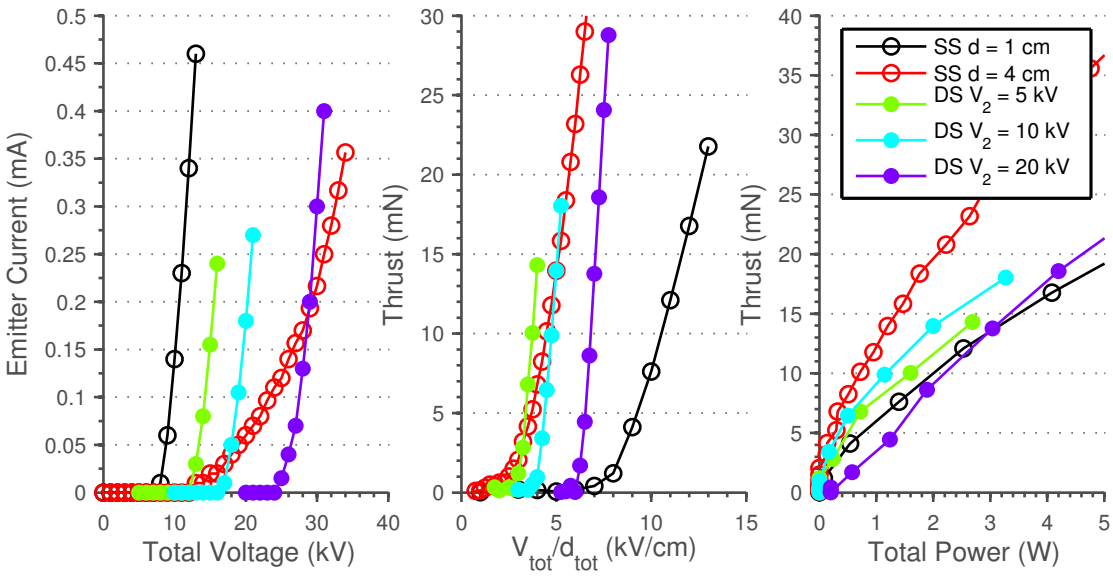

Figure 4-12: Current and thrust variation with V_2 for $d_1 = 1$ cm, $d_2 = 3$ cm

stages	Single		Dual		
case	$d = 1$ cm	$d = 4$ cm	$V_2 = 5$ kV	$V_2 = 10$ kV	$V_2 = 20$ kV
$\frac{F}{P_o}$ (mN/W)	7.78	14.36	9.68	13.66	2.02

Table 4.1: Initial thrust-to-power values for $d_1 = 1$ cm, $d_2 = 3$ cm

10 kV is, in the sense of thrust created per average field strength, equivalent to the single-stage case of the same total gap. Despite the lower required voltage, dual-stage thrusters have losses associated with ion losses at the intermediate electrode leading to reduced values of thrust-per-power, as shown in the right plot and quantified in table 4.1 using data points below 1 W of input power.

The total gap length for a dual-stage thruster can be made with different combinations of d_1 and d_2. Figure 4-13 compares two cases with a total $d = 5$ cm, one with $d_1 = 1$ cm, $d_2 = 4$ cm and the other with $d_1 = 2$ cm, $d_2 = 3$ cm. Both dual-stage cases included are for $V_2 = 10$ kV. From the voltage-current plot on the left, the $d_1 = 1$ cm design results in a higher current for a given total voltage. This plot also provides evidence to support that the first gap d_1 does in fact control the voltage-current properties of the corona discharge and thruster: although there is horizontal displacement due to the additional voltage provided by the second power supply, the slopes of the voltage-current plot are the same as their single-stage cases with $d = d_1$.

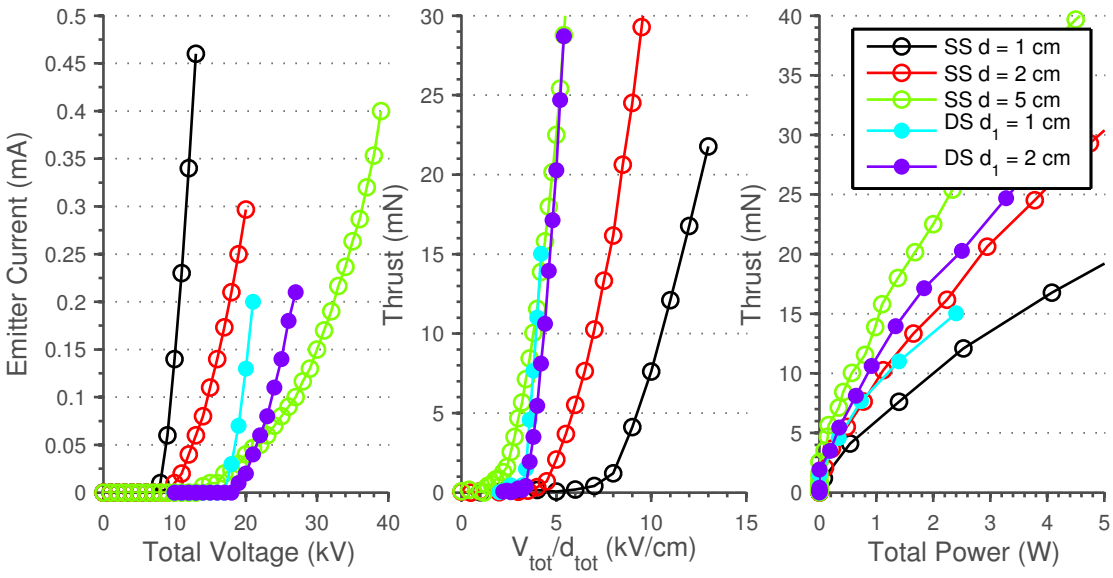

Figure 4-13: Current and thrust variation with d_1 for $d_{tot} = 5$ cm, $V_2 = 10$ kV

The single-stage $d = 1$ cm has a steeper slope than $d = 2$ cm, and the dual-stage cases reflect that trend. The effectiveness of the average field in creating thrust for the case $V_2 = 10$ kV, as in figure 4-12, is in agreement with the single-stage case for equal total gap length. From the power-thrust relationship in the right plot, it can be concluded that the presence of the second gap improves the thrust-per-power performance from the $d = d_1$ case, and that the ratio approaches the case $d = d_1 + d_2$ as an upper bound.

4.2.1 Current Distribution

The dual-stage thruster performance was expected to vary with the factor ψ, indicating the portion of the emitted current which continued past the intermediate electrode and across the second gap. The currents through all three electrodes were measured, with the currents through the emitter (I_1) and collector (I_2) read off of the power supply displays and the current through the intermediate electrode (I_0) routed through an ammeter. The factor ψ could then be calculated as $\psi = {}^{I_2}/_{I_1}$. Figure 4-14 shows the current distribution for $d_1 = 1$ cm, $d_2 = 3$ cm, and a bare intermediate electrode.

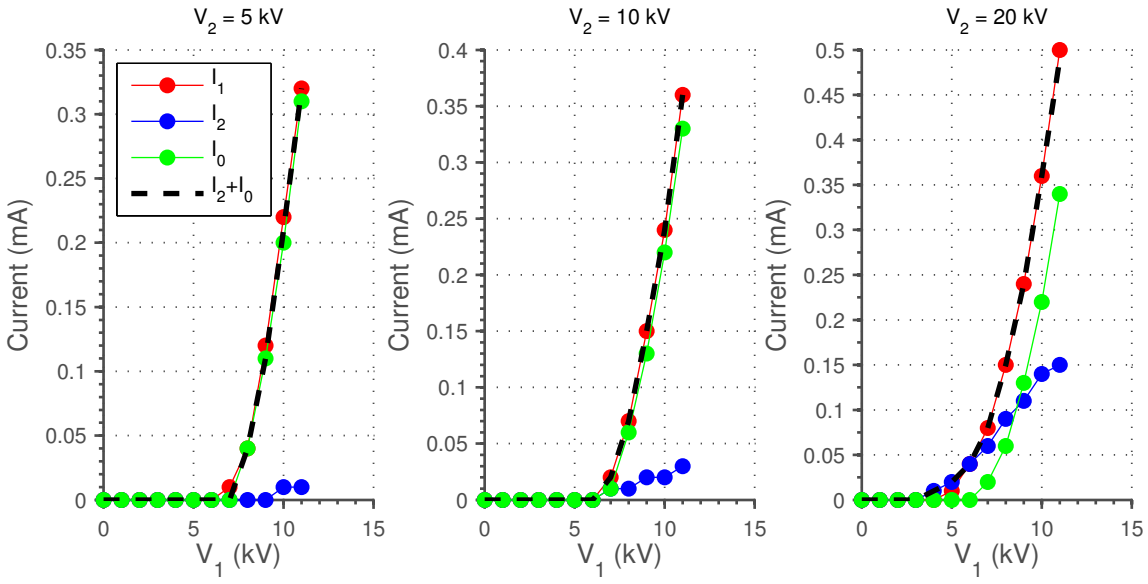

Figure 4-14: Current distribution for $d_1 = 1$ cm, $d_2 = 3$ cm, bare electrode

Clearly, ψ varies with both V_1 and V_2, with the second gap voltage showing a more pronounced effect. For $V_2 = 5$ kV, ψ remains zero until V_1 is above 10 kV, and even then is very close to zero. $V_2 = 20$ kV is the only case in which ψ becomes significant, with a value of 0.3 at the maximum thrust. This suggests that of the three cases, only $V_2 = 20$ kV is operating in a proper dual-stage condition, which explains the trend reversal seen in figure 4-10. Intuitively it makes sense for higher V_2 to increase ψ, as there is a greater field to pull the ions towards the collector instead of colliding with the intermediate electrode. If the current through the intermediate electrode could be reduced, then ψ could be raised to higher values.

Using the insulated 10 AWG wire as the intermediate electrode, the current distribution can be rearranged to allow greater ψ values. As seen in figure 4-15, ψ is 1 throughout much of the tests for all three values of V_2. However, it is important to note that the absolute value of the emitted current is greatly reduced, from a maximum observed 0.5 mA in the bare electrode case to a maximum 0.17 mA with the insulated electrode.

Looking back at the bare electrode case with $V_2 = 10$ or 20 kV shown in the center and right plots of figure 4-14, the data can be compared to theory using equation 1.28.

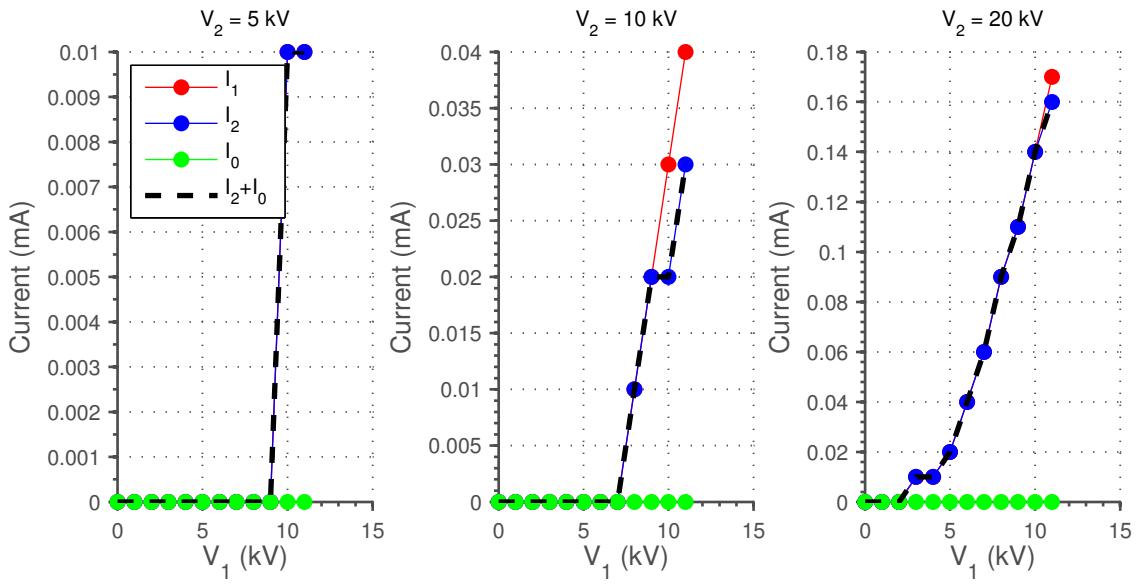

Figure 4-15: Current distribution for $d_1 = 1$ cm, $d_2 = 3$ cm, insulated electrode

Using the experimental values of V_1, V_2, and ψ in conjunction with the appropriate values of d_1 and d_2 from the geometry, the thrust-to-power ratio can be calculated. The theory is shown by the lines in figure 4-16, and the trend, as expected, is an increase in $^F/_P$ with ψ. The data also reflects this trend. The sharp corners in the theoretical curves are artifacts of the use of empirical values in the theoretical model. For $V_2 = 20$ kV, the data is shifted consistently below the predictions, but for the smaller values of V_2, the data lies within the bounds or slightly above the predictions. Although excluded here for clarity, the data for $d_1 = 2$ cm also followed the same trends.

Comparing to the right plot of 4-14 for $V_2 = 20$ kV, emitter voltages around $V_1 = 5$ kV correspond to $\psi = 1$, and as V_1 increases, both ψ and $^F/_P$ decrease. As such, in figure 4-16, the thrust increases towards the left. Several data points exist for $\psi > 1$, but this may be due to stray ionization in the lead cables connecting the collector to the negative power supply, before significant I_1 is drawn. Under ideal operation in accordance with the assumptions, the emitter generates all ions ensuring $I_2 \leq I_1$.

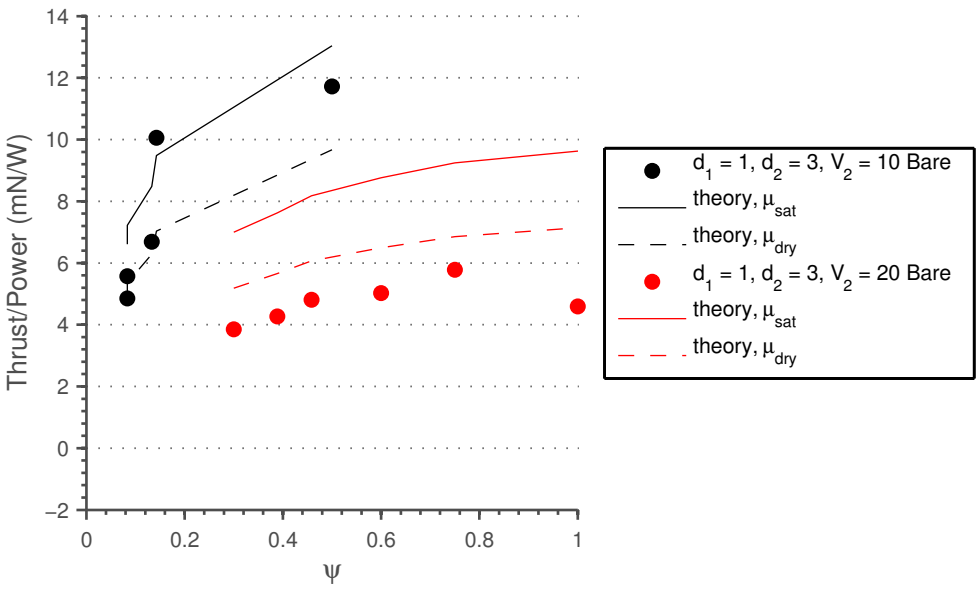

Figure 4-16: Thrust-to-power variation with ψ for $d_1 = 1$ cm, $d_2 = 3$ cm

4.3 Non-dimensional Quality

Figure 4-17 shows the variation of the quality with thrust for a subset of the single-stage thrusters. The general trend is an improvement with increased gap length. The expectation might be for all curves to trend towards an asymptote at 1, indicating the eventual agreement between theory and experiment. The data for $d = 9$ and 11 cm are consistent with this expectation.

The dual-stage thrusters show more consistent trends. For the cases where $V_2 =$ 5 or 10 kV (left and center plots in figure 4-18), all configurations show decreasing quality as thrust increases. Furthermore, as d_2 increases, the quality is reduced. Changes in d_1 and d_2 affect the quality differently, as the $d_1 = 2$ cm consistently shows higher quality than the 1 cm design with the same d_2. The dependence on d_1 is amplified by a smaller d_2, with an average difference in quality of ≈ 0.3 for $d_2 =$ 3 cm, as opposed to ≈ 0.15 for $d_2 = 13$ cm with $V_2 = 5$ kV. $V_2 = 10$ kV shows a larger spread with configuration than the $V_2 = 5$ kV cases. The worst configuration with both voltages, $d_1 = 1$ cm and $d_2 = 13$ cm, show a similar asymptote near 0.1. However, the best configuration of $d_1 = 2$ cm and $d_2 = 3$ cm shows a quality of $\approx$ 0.75 at $F = 25$ mN for $V_2 = 10$ kV as opposed to ≈ 0.6 at the same thrust level for

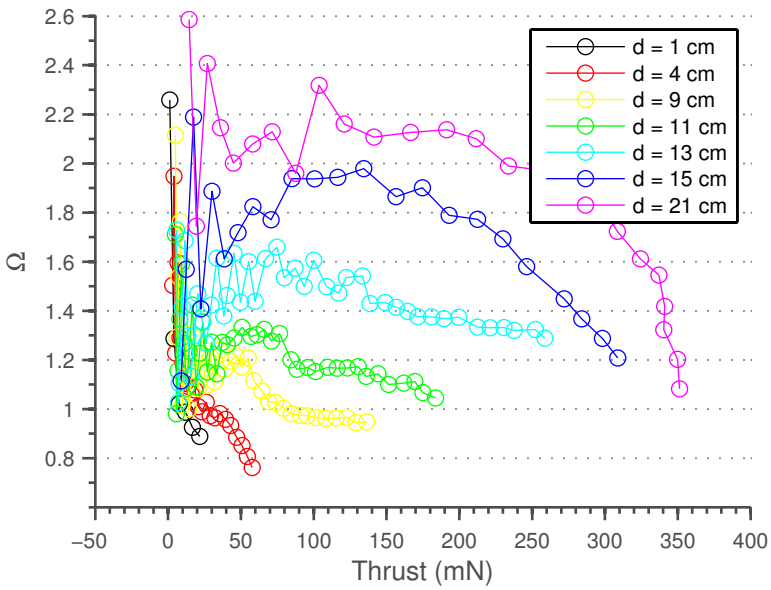

Figure 4-17: Variation of ND quality with thrust, single-stage

$V_2 = 5$ kV.

For $V_2 = 20$ kV (right plot of figure 4-18), some of the trends shift. In the cases of $d_2 = 3$ or 4 cm, the quality increases with thrust to an asymptote in the 0.5 to 0.6 range. The longer gaps show quality decreasing with thrust, with the $d_2 = 6$ cm case tending towards asymptotes around 0.4 and the $d_2 = 13$ cm dropping below 0.3.

Figure 4-19 compares single-stage and dual-stage thrusters of equal total length $d = d_1 + d_2 = 5$ cm. The single-stage cases consistently show a higher quality than the dual-stage cases. This is expected given the low values of ψ achieved with these dual-stage thruster configurations.

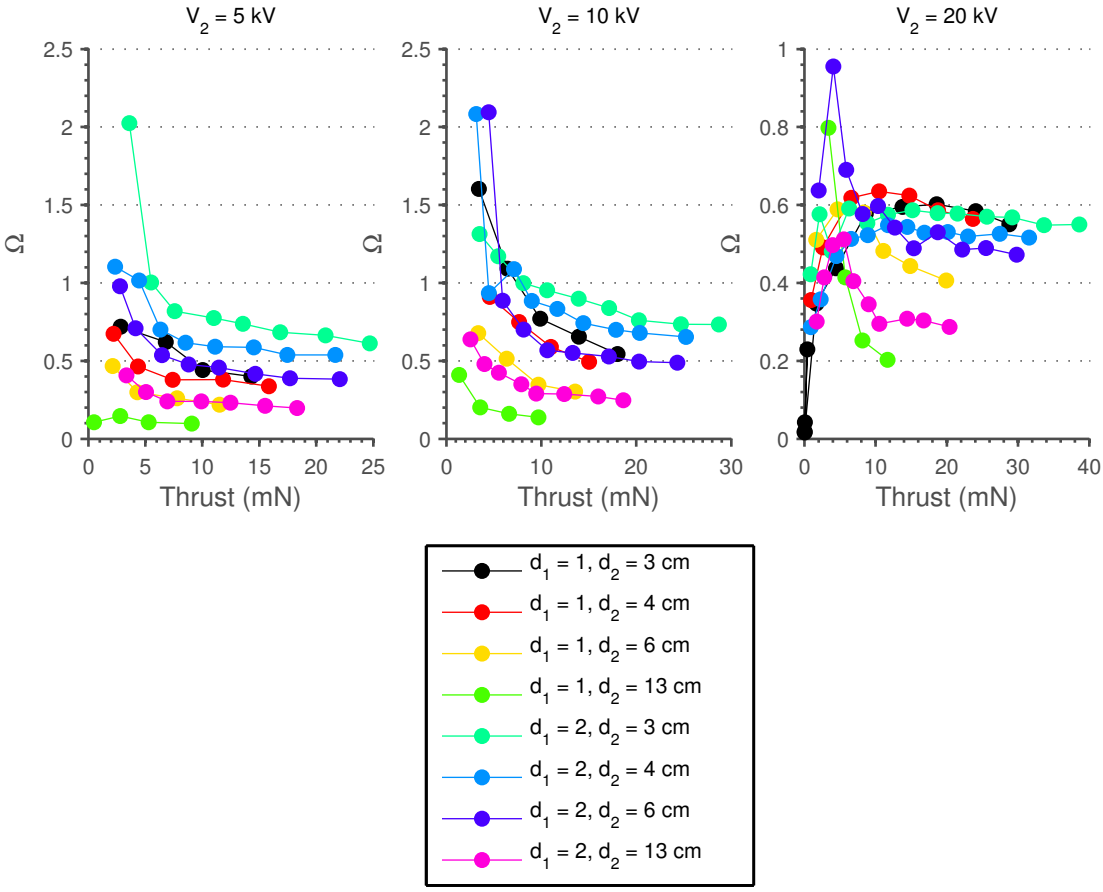

Figure 4-18: Variation of ND quality with thrust, dual-stage

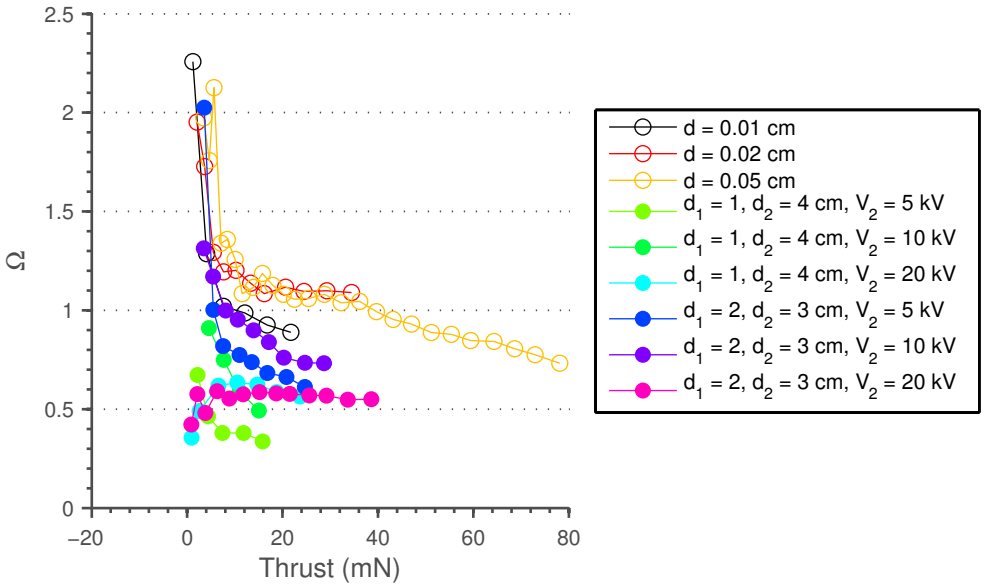

Figure 4-19: Quality comparison between single- and dual-stage with $d_{tot} = 5$ cm

Chapter 5

Conclusions

This thesis presented the performance characteristics of single- and dual-stage electrohydrodynamic thrusters, and how they varied as the gap lengths were changed. Many of the trends predicted by the one dimensional theory were confirmed.

The single-stage thrust F was confirmed to vary proportionally with $\frac{V(V-V_o)}{d}$ for gaps up to $d = 9$ cm. Beyond this gap, the quadratic form in voltage is retained, but the variation with d reverses trends and larger thrust is produced at a given voltage with longer gaps. The exact cause of this trend reversal is undetermined, although one possibility is the divergence of the design from the assumption that the electrode lengths were infinite, or practically much greater than the next significant length scale given by the gap distance. Design in this reversed trend regime offer higher thrust for a given voltage and a better thrust-to-power ratio.

The linear relation of current I with the quadratic term in voltage $V(V - V_o)$ was observed, and the line is broken into two pieces with a higher slope beyond the onset of the reverse current as predicted by the bilinear theory. The linear dependence of thrust on current, again subject to the bilinear theory's performance loss, was confirmed, in agreement with the sum conclusion from the previous two points of $F \propto \frac{V(V-V_o)}{d}$ and $I \propto V(V - V_o)$. Furthermore, the actual thrust measurements were in agreement with the theoretical predictions made using the empirical values of ion mobility.

The thrust-to-power ratio was confirmed to increase with gap length, with a max-

imum measured value (averaged for the points corresponding to $P < 1$ W) of 68 mN/W with $d = 21$ cm. Both current and power were seen to decrease inversely with gap length in generating the same thrust force. This shows that larger gaps, especially in the regime with the reversed voltage-thrust trend, require a smaller power supply for a given target thrust. However, as the gap is increased further, the decrease in electrical power requirement per unit increase in gap length is diminished.

The bilinear theory made accurate predictions on the location of the sharp degradation in performance. The thrust-to-power ratio predictions generally overestimated the performance, and further loss mechanisms are expected to exist especially at higher power levels.

The dual-stage thrusters were compared to single-stage thrusters under two separate paradigms: 1) maintaining similar electrical characteristics by comparing $d = d_1$, and 2) maintaining similar volumetric requirements by comparing $d = d_1 + d_2$. In the first sense, adding larger second gaps proved effective in all cases at reducing the average electric field strength required to generate a given thrust. However, only the $V_2 = 20$ kV was effective in increasing the thrust-to-power ratio at larger gap lengths, which was expected to be the case for dual-stage designs. This, combined with the current distributions amongst the three electrodes, showed that second gap voltages as high as 10 kV were not high enough to ensure proper dual-stage operation with significant current across the second gap. The slope of the thrust-to-power variation with increasing d_2 was found to match the theoretical predictions, but losses unaccounted for in the theory shifted the actual values of the thrust-to-power ratio lower.

The second set of comparisons revealed a tradeoff in using a dual-stage design as opposed to a single-stage design of the same total gap. Adding in the intermediate electrode increased the effectiveness of the thruster in drawing current for a given total voltage. However, the presence of the intermediate electrode induced losses, including the significant portion of current which was collected by the grounded intermediate electrode thereby allowing a smaller number of ions to cross the second gap. This ultimately resulted in a smaller thrust-to-power ratio for the same total gap length.

Using this electrode geometry, a dual-stage design allows for lower overall voltage in generating a given thrust, but requires more current and thus higher power. A way to mitigate these losses is to increase ψ, the ratio of current across the second gap to the current generated at the emitter. Using an insulated intermediate electrode allowed for operation at or near $\psi = 1$, but was less effective at drawing current flow. A rearrangement of electrodes to better shape the electric field and allow for more current to pass beyond the intermediate electrode will allow for higher values of ψ, leading to improved thrust-to-power ratios.

The nondimensional quality Ω was used to assess the geometries of single- and dual-stage thrusters. The single-stage thrusters with gaps larger than $d = 11$ cm showed higher performance than expected, possibly corresponding to the reversal of trends in the voltage-thrust characteristic. Dual-stage thrusters behaved more consistently, with most cases showing a reduction in quality with increases in thrust and d_2. Only the $V_2 = 20$ kV with $d_2 = 3$ or 4 cm cases showed increasing quality with thrust. For thrusters of equal length, single-stage thrusters consistently demonstrated higher quality than the dual-stage configurations.

5.1 Recommendations for Future Work

Electrohydrodynamic thrusters are still at an early developmental stage. Much further investigation is necessary in order to determine the practicality and potential of this technology.

One important factor for gauging its practicality is thrust density. Previous works on EHD thrusters and this thesis focused on the air gap as the geometric variable. Although Christenson gave values for thrust/area [10], the physical area of the thruster setup did not change. The effects of multiple electrode pairs operating in proximity must be studied, with consideration of how the field lines are affected and how much losses are induced from neutral particles colliding with the additional surface area of electrodes. Another important three-dimensional effect to be studied is end effects, namely the physics at the ends of linear thrusters like that used in this thesis or at

the corners of triangular or other polygonal thruster geometries. With the current design EHD thruster, a metric could be thrust per electrode length.

In order to study the aforementioned 3D effects, it may be prudent to create more sophisticated electric field simulations. The MATLAB PDE Toolbox tool included in appendix B was two dimensional and only applicable for small currents with negligible space charge effects. A 3D simulation accounting for space charge will be useful in predicting the performance of using more electrodes or electrodes laid out in different arrangements.

A method to better shaping the electric field geometry would be useful in improving thruster performance. The main known loss mechanisms for EHD thrusters are ionization energy losses, cosine losses in the collision momentum transfers, Joule heating of the ambient gas, and the reverse component of thrust due to the bilinear effect. With better control of the field geometry, the cosine losses due to the horizontal component of the field as well as the bilinear effect may be mitigated. The dual-stage study in this thesis, in a manner, was a way to reshape the field in order to induce current with lower overall voltages. The wire-cylinder-plate geometry used by Colas was another example of reshaping the field, effectively creating field lines parallel to the centerline and thus reducing the cosine losses [11]. Also, the use of an external electric field as explored in Appendix D should provide further flexibility.

A last recommendation would be to study other mechanisms of separating the ionization and acceleration phases of electrohydrodynamics. Several studies have considered AC or pulsed DC excitation in order to accomplish this [18] [25]. Another way would be to employ different plasma generation techniques, such as radio-frequency generated plasma. An RF plasma generator could be used in conjunction with a low voltage air gap to operate as a kind of dual-stage thruster.

Appendix A

Additional Plots and Data

d (cm)	V_o	V_{o2}	I_{o2}	a_1	a_2	$\frac{F}{P_o}$ (+)	$\frac{F}{P_o}$ (-)
1	6.92	11.00	0.25	53.88	41.69	7.78	5.57
2	7.61	15.01	0.13	126.44	115.80	10.73	9.70
3	8.28	19.00	0.11	186.15	146.86	13.19	11.99
4	9.54	27.00	0.16	216.02	118.96	14.36	13.19
5	11.14	29.00	0.14	286.48	157.78	16.04	17.89
7	12.40	34.00	0.12	385.31	229.53	17.69	20.02
9	14.66	39.00	0.11	566.91	412.65	21.77	25.10
11	15.72	42.00	0.10	749.74	568.38	25.54	30.87
13	16.92	46.00	0.10	1061.9	810.83	30.36	32.39
15	18.47	48.00	0.10	1514.9	691.92	44.28	48.43
18	17.99	52.00	0.10	2035.0	848.12	58.85	56.24
21	19.49	52.00	0.10	2374.0	616.91	68.43	

Table A.1: Single stage thruster properties

Table A.1 summarizes various measured values for single-stage thrusters. Included are the corona inception voltage as calculated from the x-intercept in the I vs $V(V - V_o)$ plot, the secondary corona inception voltage and current from the bilinear effect, the slopes of the two linear fits for the voltage-current relationship in the bilinear analysis, and the initial thrust-per-power ratios for points with power less than 1 W.

Figure A-1 shows three trials for a single-stage thruster with gap length $d = 1$ cm. The agreement between the three data sets indicates the extent of the reliability in the data measurement technique and allows for the use of averaged data, as done in the main results section of this thesis. Furthermore, the repeatability demonstrates that

with proper ventilation time between trials, the hysteresis seen in the up-and-down pretrials have no persisting effects across trials.

Figure A-2 shows the quadratic relationship of thrust with voltage, as predicted by equation 1.21. Cases of longer gap lengths were excluded for clarity. For the higher gap lengths, the bilinear effect increases in prominence and distorts the linear relationship. This distortion is visible in the included cases as well, for example at around $V(V - V_o) = 400$ in the $d = 7$ cm case.

Figure A-3 shows the overperformance of the single-stage thruster beyond theoretical predictions. The case shown here is for a gap of $d = 21$ cm. Gap lengths up to $d = 11$ cm are well contained within the theoretical bounds, but at larger gaps, the thrust is higher by as much as 66% than expected. A possible cause for this is the deviation from the $L \gg d$ approximation in the one dimensional theory derivation.

Figure A-4 compares the current draw for a given voltage with positive and negative polarity coronas. The negative polarity draws a higher current at each voltage, with the maximum mean standard deviation for the five gaps shown of 0.016 mA over the appropriate voltage domain. Larger gaps were omitted for clarity.

Figure A-5 compares the thrust as a function of voltage between the positive and negative polarity excitations. The performances show a higher thrust per voltage with the negative corona, by a mean standard deviation of 0.48 mN over the domain for $d = 1$ cm case and 1.40 mN for $d = 5$ cm. Higher gap lengths were omitted for clarity, but follow the same trends.

Figure A-6 compares the thrust as a function of current between the positive and negative polarity excitations. The negative ions are less effective at transferring its energy into the neutral molecules, as the negative ion current systematically generates less thrust per amp. Mean standard deviations ranged from 0.485 mN to 1.403 mN over the appropriate domains for each gap length. Larger gaps were omitted for clarity.

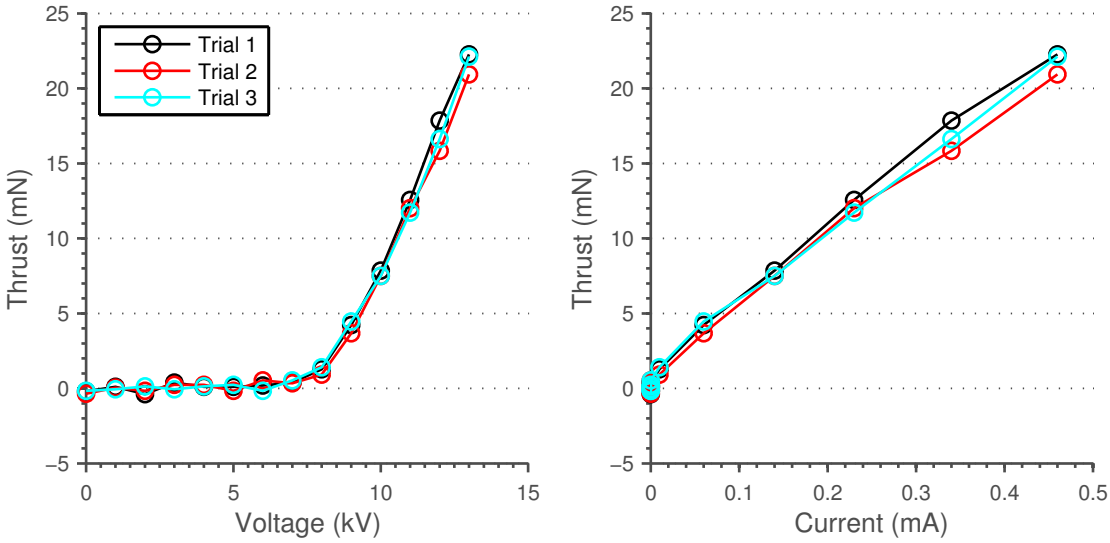

Figure A-1: Repeatability of experimental data

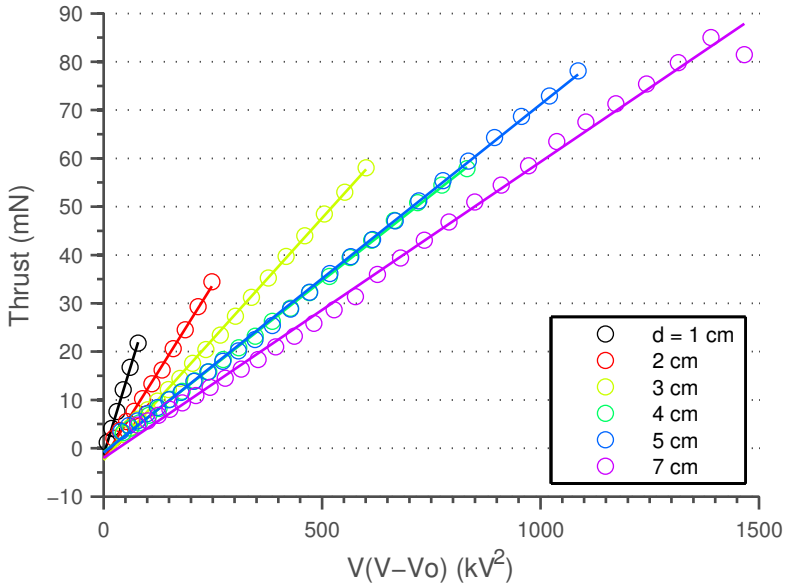

Figure A-2: Linear relationship of thrust and $V(V - V_o)$ for single-stage thrusters

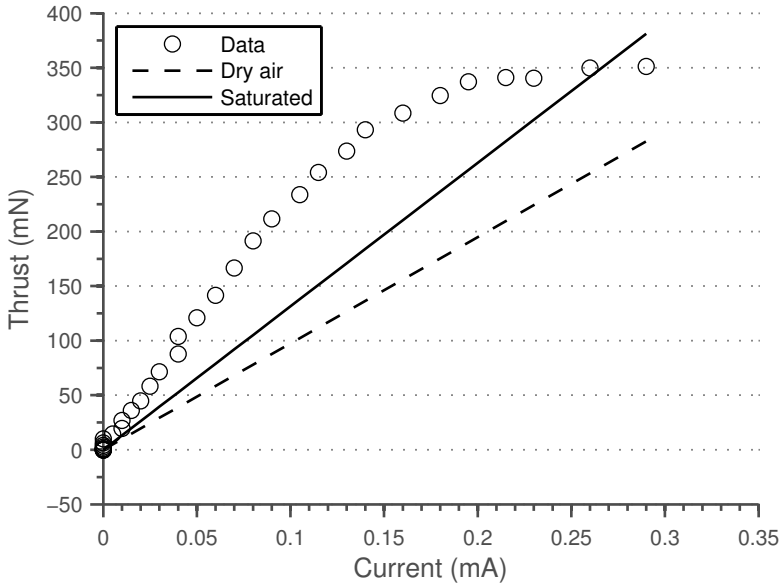

Figure A-3: Performance of large gap single-stage thrusters compared to theoretical prediction

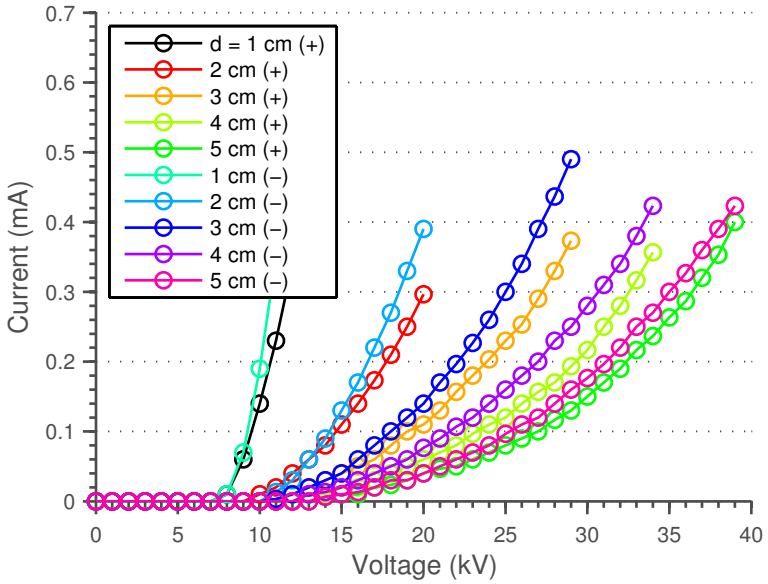

Figure A-4: Negative polarity excitation draws larger current at a given voltage than positive polarity

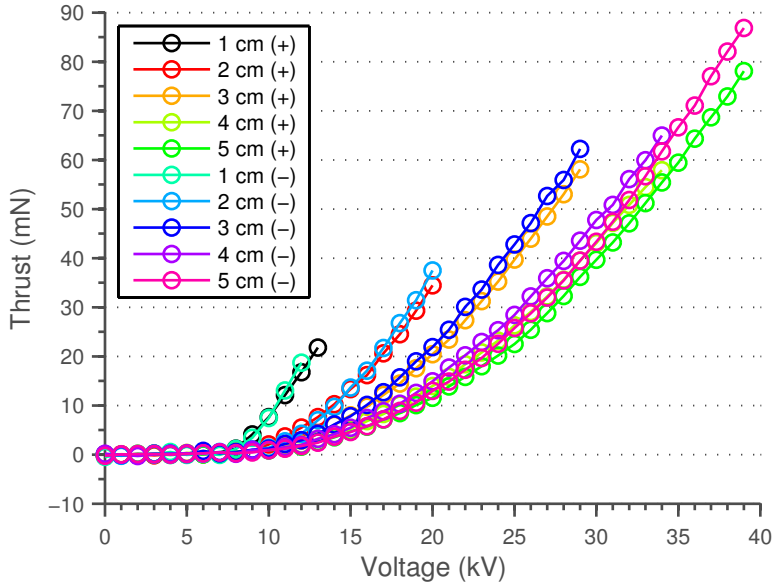

Figure A-5: Negative polarity excitation generates higher thrust at a given voltage than positive polarity

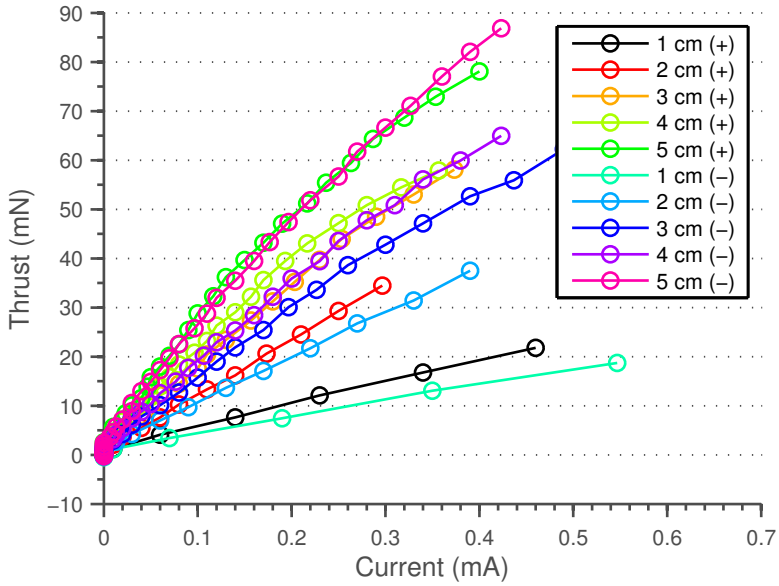

Figure A-6: Positive polarity excitation generates higher thrust for a given current than negative polarity

Appendix B

Electric Field Simulation

The MATLAB Partial Differential Equation Toolbox was used to simulate the electric field around the thruster. The tool does not factor in the effects of space charge, and thus the results become more inaccurate as current and corresponding space charge increases.

B.1 Single-stage Thruster

The tool for the single-stage thruster takes two inputs, the gap length and emitter voltage, and uses the appropriate geometry for the thruster. The colormap corresponds to the electric potential or voltage, and the values are given by the colorbar on the right. The arrows show the direction of the electric field, and their lengths correspond to their magnitude. Figure B-1 is the output for a $d = 4$ cm, $V = 13$ kV case.

The electric field in the gap points from the emitter towards the collector, although they take on a horizontal component as their distance from the centerline increases. The ions in the corona discharge current travel along the field lines, tangential to the arrows. During this process, neutral molecules gain momentum through collisions with the ions. Due to the symmetry of the field lines, no net horizontal component is expected in the thrust; the y-component of the electric field contributes to the net thrust. The voltage colormap shows a very sharp decrease in potential near the

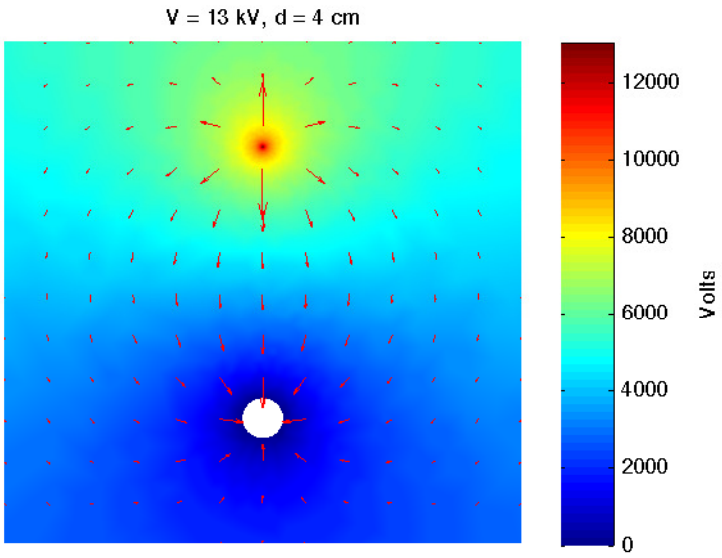

Figure B-1: Electric field simulation for $d = 4$ cm, $V = 13$ kV

emitter. This strong gradient, corresponding to the longest arrows (highest electric field magnitude), causes the ionization and ignites the corona discharge.

B.2 Dual-stage Thruster

The dual stage version of the tool takes four inputs, the two gap lengths and two voltages, and uses the appropriate geometry for the thruster. As in the single stage tool, the colormap gives the voltage and the arrows give the local electric field vector. Figure B-2 shows the output for a $d_1 = 1$ cm, $d_2 = 3$ cm, $V_1 = 8$ kV, and $V_2 = -5$ kV case.

The electric field points from the emitter towards the collector, bypassing the intermediate electrode except for the field lines directly in line with the electrodes. Compared to figure B-1 with the single stage electric field simulation for the same total gap and voltage, the electric field vectors show several distinctions. The field vectors above the emitter or below the collector, which point in the wrong direction for thrust production, are of a smaller magnitude. The field vectors in the gaps are also smaller in magnitude than in the single stage case, but they show better

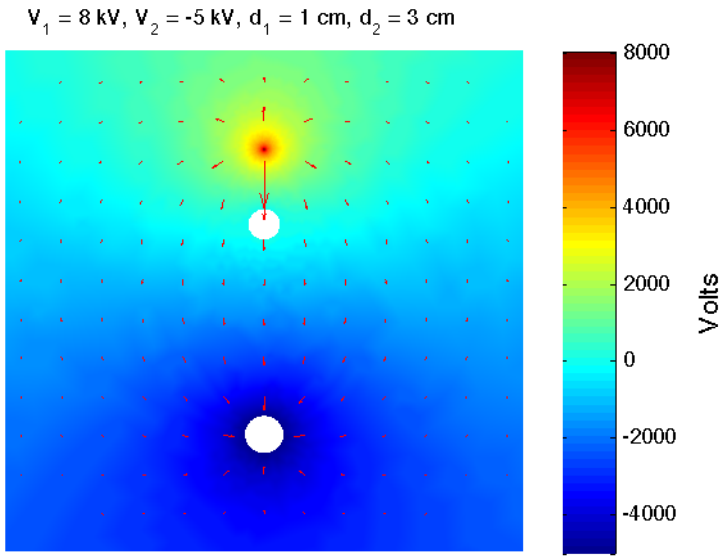

Figure B-2: E-field simulation for $d_1 = 1$ cm, $d_2 = 3$ cm, $V_1 = 8$ kV, $V_2 = -5$ kV

vertical alignment, which suggests a tighter plume and more directional efficiency in momentum transfer between particles. The voltage colormap shows the sharpest potential difference in vicinity of the emitter. This suggests that the ionization and subsequent corona discharge will occur at the wire emitter.

Appendix C

Lifter Setup

Before working with the table and frame setup, experiments were run on a more conventional triangular "lifter" design. A thruster was built based on Payton's design [20] on a balsa wood frame, with an aluminum foil collector and the same 35 SWG wire emitter. The final weight of the thruster was roughly 9 g. A bending-beam load cell was specially designed to test this thruster. However, several issues were discovered throughout testing this device, which led to noisy and unreliable data. Lessons learned from this experiment directly led to the design of the frame thruster. This chapter will discuss the construction and results of the lifter setup, and summarize the issues which arose due to the design.

C.1 Construction

The basic design of the lifter setup followed the specifications from Payton [20] and Miller [18]. An equilateral triangular frame with sides 20 cm in length was constructed from balsa rods. Vertical supports were attached at each corner, each 17 cm long. The triangular frame was supported 4.5 cm from one end of the vertical rods, with the longer side notched at 1 cm increments to hold the emitter wire. A plastic straw with radius 3.4 mm was placed around each of the sides, so as to give a smooth surface to attach the collector foil onto. The collector was a rectangular piece 9 cm $\times$ 19.5 cm cut from a household aluminum foil, folded around the straw in a crude airfoil

shape. The emitter was the same 35 SWG wire used in the table and frame setup. A single wire was wrapped around the frame in the appropriate notches along the vertical supports, with one end of the wire extending out to allow a connection from the high voltage power supply.

Figure C-1: 3-view for load cell design

In order to measure thrust, a custom bending beam load cell was designed as shown in the three-view of figure C-1. The beam was a $28.77 \times 2.54 \times 0.32$ cm PVC piece, designed for a maximum load corresponding to 0.4 N, a combination of the weight and downward thrust from the thruster. With four strain gauges placed 6 cm from the root in a full Wheatstone bridge configuration, the maximum expected strain was 1 millistrain at a deflection of 2.17 cm. PVC was selected for the beam for its electrically insulating property and small modulus. As the beam would be in proximity to the emitter wire, a nonconducting material was necessary. Also, due to the small forces expected from previous measurements by Payton, the small modulus was favorable for ensuring good resolution in thrust. A balsa support was attached to the tip of the bending beam as a fixture onto which the thruster could be attached. Cotton strings were used to connect to the vertical supports of the thruster above the collector. Figure C-2 shows the complete load cell.

The wires from the strain gauges were connected to a National Instruments NI9237

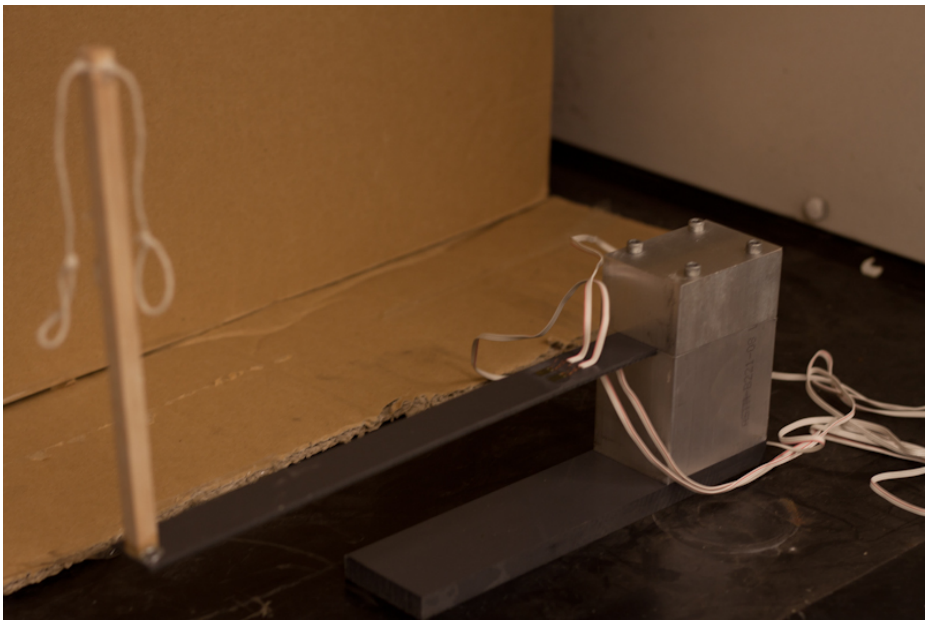

Figure C-2: Bending beam load cell

Bridge Module through a NI 9949 screw terminal. The bridge module communicated via USB with a computer running LabViewSE, which recorded strain. This strain was then converted into a force, using a linear fit determined by tests with known weights.

C.1.1 Electrical Layout

The circuit for the lifter tests used the same layout shown in figure 3-5 for the table and frame setup. However, only the positive polarity power supply was used. The power supply output was connected with an alligator clip to the wire emitter, and another small piece of wire was attached to the foil collector to be connected to the ground.

Preliminary tests for a dual-stage design were also conducted with the lifter setup. In this case, as only one power supply was available, a resistor chain was used to provide two separate potentials. The collector was kept grounded, the high voltage output was directly connected to the emitter, and some intermediate voltage was routed to the intermediate electrode. Two 35 SWG wires were used for the emitter and intermediate electrode, each wrapped around the frame using the notches as in

the single stage case. The dual-stage layout is illustrated in figure C-3.

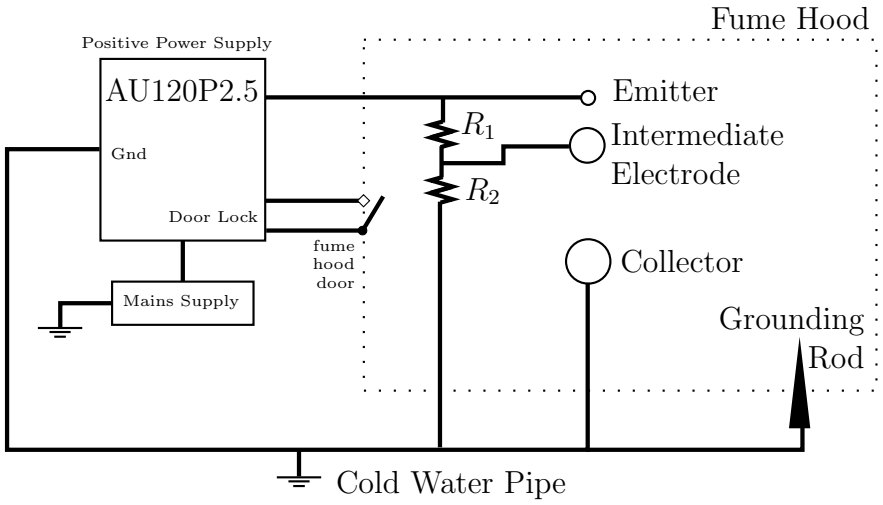

Figure C-3: Lifter setup dual stage circuit diagram

The two resistances shown, R_1 and R_2, were comprised of a chain of resistors totalling 60 MΩ. A wire with alligator clips on both ends connected the intermediate electrode to the appropriate point in the resistor chain, so the ratio $^{R_1}/_{R_2}$ could be adjusted.

C.2 Results

A summary of the results will be presented. All of the observed trends are consistent with those presented in the main paper, although the absolute values differ due to differences in geometry, most notably the total electrode length of 60 cm as opposed to 40 cm.

C.2.1 Experimental Procedures

The tests were similar to the single-stage tests in the table and frame setup. A gap length was chosen and the emitter wire adjusted accordingly. Then, the applied voltage was raised in 1 kV increments until arcing, with voltage, current, and thrust measured at each increment.

In the dual-stage case, in addition to the geometry, the resistance ratio was selected before each trial. The actual voltage applied to the intermediate electrode changed at each increment, and this was calculated using the resistance ratio.

C.2.2 Thruster Performance

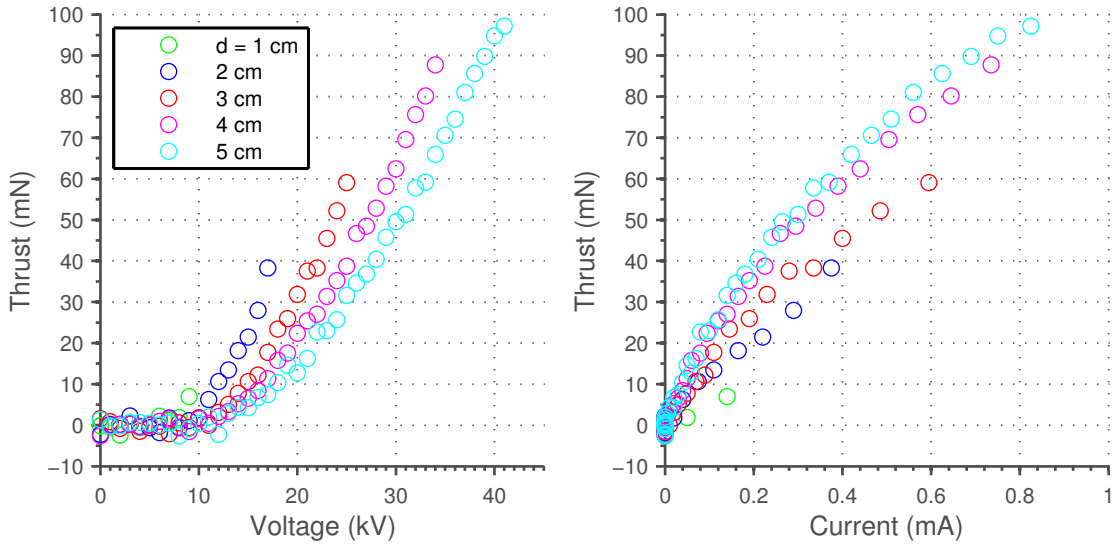

Figure C-4: Lifter thrust dependence on voltage and current

As in the case of the frame thruster setup, the force vs voltage plot in figure C-4 shows a shift towards the right as the gap length increases. This corresponds to a higher inception voltage for the corona discharge. The maximum gap tested with this setup was 5 cm, too small to verify the reversing of the trend seen at larger gaps in the frame thruster. Plotting the thrust vs $V(V - V_o)$ showed a linear fit, supporting equation 1.19.

The thrust vs current plot in figure C-4 is also similar to the frame thruster case, showing an increase in thrust output for a given current with larger gap. Plotting the square root of current vs voltage also showed linear dependence, as predicted by equation 1.18. The data shows a decrease in the performance at currents higher than about 0.1 mA, as predicted by the bilinear performance theory. The point where the performance shifts is indicated in figure C-5 with a solid square point. Figure C-6

shows the fits to the current-thrust relationship and the bilinear model predictions for the power-thrust relationship.

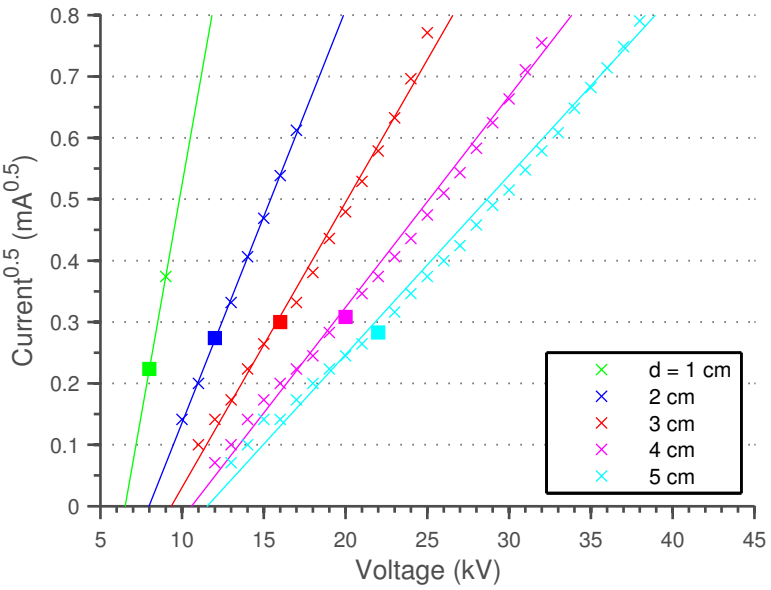

Figure C-5: Lifter current dependence on voltage

C.3 Lessons Learned

As indicated by the error bars in figure C-7, the lifter setup data showed significant noise. The largest error range is close to spanning 20 mN. Running the experiments inside the fume hood was necessary for safety considerations, but the rough airflow had a significant effect on the thruster. The thruster was very light, and the foil collector created a large surface area to be pushed on by the fume hood flow. Furthermore, the strain gauges were very sensitive, picking up on the oscillations caused by the fume hood flow.

These issues were overcome by several design decisions in the frame thruster. First, the collector was replaced by a tube, which poses a significantly smaller surface area than the foil. Second, the overall thruster was made much heavier, so that it would be more robust to being tossed around by the fume hood flow. Also, the load cell employing strain gauges was replaced by a digital scale, which was set to record

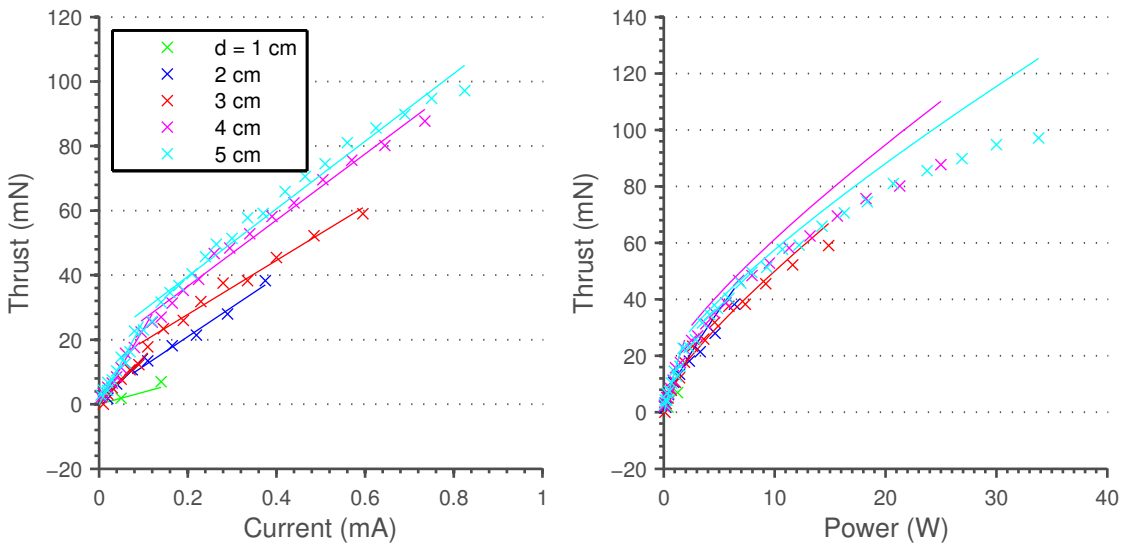

Figure C-6: Lifter bilinear performance

an output only after the reading stabilized to within the 0.01 g accuracy of the scale.

The preliminary dual stage tests did not show the performance expected from a dual stage design. One reason was that the same radius wire was used for both the emitter and intermediate electrodes. With the corona inception voltage across this gap, there is little preference for the corona discharge to form around the emitter. The electric field is affected by the presence of the collector and thus the corona does form first around the emitter, but a reverse corona forms quickly around the intermediate electrode as well, showing the decreased bilinear performance. For the frame thruster, a much larger intermediate electrode was used, in the form of a 4 AWG wire, almost as large as the collector tube.

Another problem with the dual stage lifter design was the use of the resistor chain. Although this was able to create an intermediate voltage, the exact value of that voltage was difficult to determine. Similar amounts of current were flowing through the resistor chain and the corona discharge, and thus the voltage divider equation could not be used reliably to calculate the intermediate electrode potential.

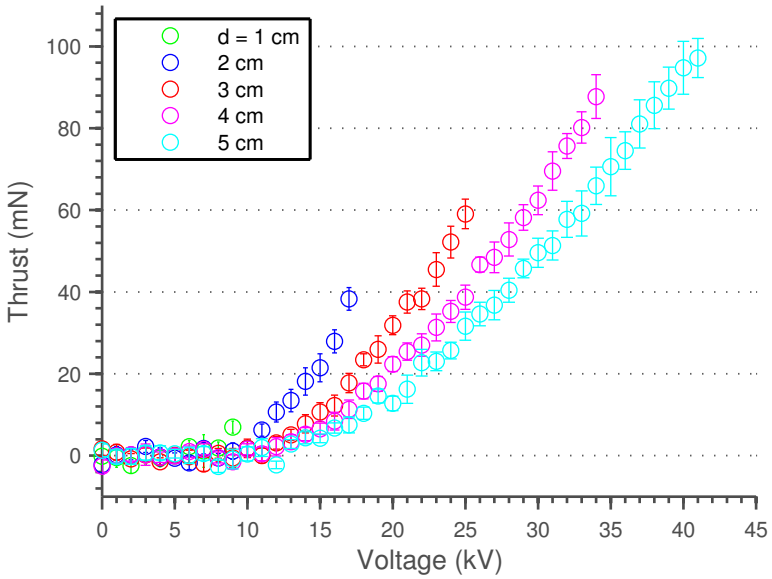

Figure C-7: Error bars for lifter data

Appendix D

Wiring Layout Performance Change

As the single-stage tests on the table and frame setup were conducted at larger gaps where voltages exceeded 50 kV, the insulated lead wire connecting the power supply output to the emitter electrode started to leak current. In particular, streamers were observed between the wire and fume hood floor, as well as between the wire and the water faucet inside the fume hood. In an effort to reduce these losses, the lead wires for both positive and negative power supplies were cut down in length so as to allow more separation with those features. In the original wiring layout, the lead wire was taped along the table leg to the crossbeam support; the shortened wire was instead routed straight to the crossbeam. As the wires were supposed to be fully insulated, these changes were not expected to affect the experimental results.

The tests being conducted at the time of these adjustments were for a gap length of $d = 9$ cm. Tests conducted immediately following the changes showed significant decreases in the thrust output. Ambient effects, including temperature and humidity, were determined not to be the cause, as the reduced performance was repeated over multiple trials under different weather conditions. The reduced thrust output was observed for smaller gaps and for both polarities.

A series of tests were conducted in order to determine the exact cause of the performance loss. First, all components were cleaned and returned to their original

conditions. The aluminum tube collector was wiped down with isopropyl alcohol, and the wire emitter was replaced with a new length of the same wire. The PTFE frame was wiped down as well. The plastic sheets making up the table top and front surfaces were flipped around, so that any surface effects which may have built up from previous exposure to ionized products and ozone could be ruled out. These changes resulted in no significant performance changes.

Next a series of tests was conducted with different wire configurations. Various wires were used to connect the high voltage power supply output to the emitter. Some of these wires did not have clips, so a combination of alligator clips unattached to anything and alligator clips at the ends of other wires ostensibly not serving any purpose were used. However, it was found that some wire configurations involving this other wire resulted in the higher performance seen before the lead wire shortening.

Twenty trials were run with this alligator clip and attached wire. Eight of the twenty trials showed the improved performance on par with that from before the wire shortening, and the rest showed the reduced performance. There was some variation within each group, but as shown in figure D-1, they were clearly separated into two groups. The voltage-current relations were consistent for all trials.

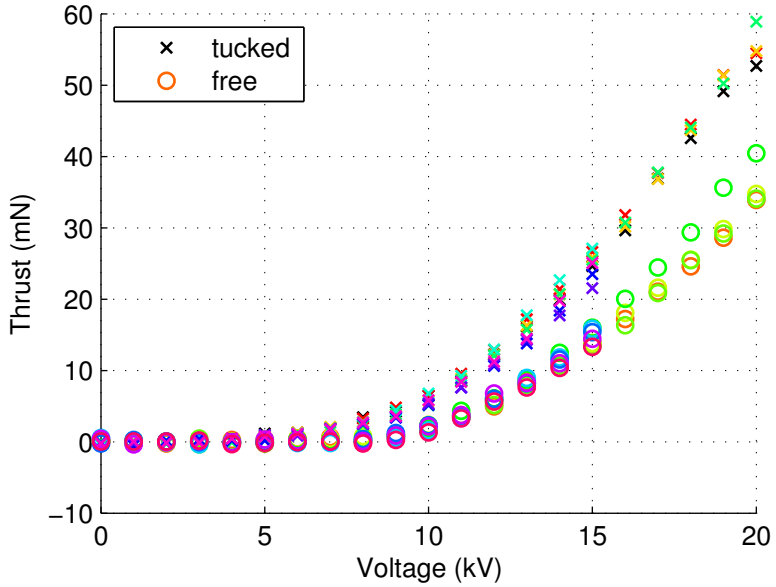

Figure D-1: Performance change dependent on wire layout

The common feature amongst the eight higher performance trials was that the other end of the attached wire was tucked into a piece of electrical tape used to hold the plastic crossbeam onto the table leg. The other twelve cases had left the other end of the wire dangling free, outside of the working area underneath the table. The wire connection to the table leg may be an analogue to the unshortened lead wires running along the table leg in the original wire configuration, which showed the higher performance. Several hypotheses were formulated for the role this extra wire may have played.

1. Ionization in the electric field created between the wire and the wooden leg fed additional ions into the thruster field,

2. The wood leg was raised to some potential between zero and the wire voltage, inducing an electrostatic interaction with the thruster

   (a) Electrostatic interaction between the table and collector,

   (b) Electrostatic interaction between the table and emitter,

   (c) Electrostatic interaction between the table and ion cloud.

Tests were conducted to test each of these hypotheses with the exception of the interaction between the table and ion cloud, which could not be run independently of the collector and emitter. In order to test for the ionization between the wire end and wooden leg, an ammeter was placed in series with the wire. Trials were run with both the tucked and free-floating wire ends, with the performance changing as above. In both cases, zero current registered on the ammeter, indicating no ionization at the wire end to within the 0.01 mA resolution of the ammeter.

In order to test for the interaction between the table and collector, the emitter wire was removed. The extraneous wire in question was tucked or left dangling as in other trials, and the collector, instead of being grounded, was connected to the negative power supply. The wire was raised to a constant 10 kV, and the collector varied from 0 to -15 kV. Throughout the range of measurements, no discernible thrust was observed.

In order to test for the interaction between the table and emitter, the collector was removed. In its place, a balsa beam was added in order to maintain structural rigidity. Although the collector aluminum tube was removed, the sprig pin leads which served as the electrical conduit to the ground were still present and grounded. At higher voltages, a current of 0.01 mA was registered as well as corresponding thrust, created by electrohydrodynamics between the emitter and the sprig pins. In these tests, the extraneous wire being tucked caused a significant level of thrust to be generated, which is unseen in the free-floating case. In order to see how this force compared to the performance loss observed in the full thruster tests, the results from several trials were compared. The forces seen in a full thruster with the extra wire untucked was added to the forces seen on the emitter with the wire tucked, and the forces from the emitter with untucked wire was subtracted so that the small EHD thrust at higher voltages would not be double counted. These results were compared against a full thruster with tucked wire, shown in figure D-2.

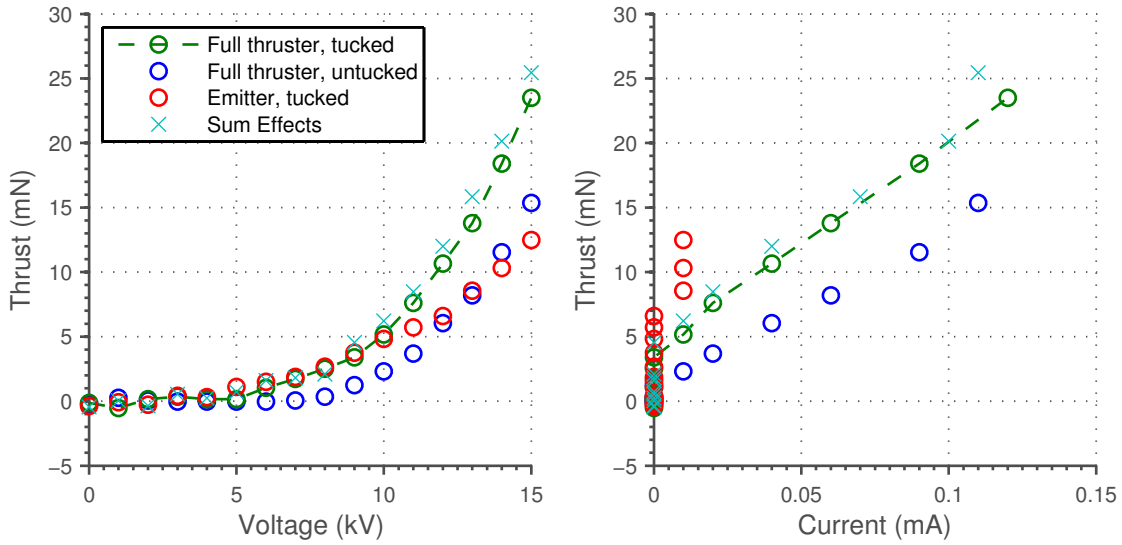

Figure D-2: Full thruster (untucked) + emitter effects compared to full thruster (tucked)

The sum of the forces match well with the full thruster with tucked wire case in both voltage-thrust and current-thrust relationships. The total current output as a function of voltage also matches between the sum and the full thruster with tucked

wire. These results indicate that there is an interaction between the table and the emitter as a result of the wire connection from the power supply to the table leg. Voltmeter probes were attached at various points on the table in order to better understand the exact nature of the interaction, but the readings never stabilized and often overloaded the capacity of the voltmeter used.

The data presented in the main portion of this thesis was measured with the lesser performance configuration. The higher performance seen before the lead wire was shortened is believed to be a result of an external electric field created by the table being raised to some potential. This suggests a potential method of increasing EHD thruster performance using an externally supplied field. If the nature of the performance change explored in this chapter can be better understood, it offers a way to significantly improve both thrust and thrust-per-power (the voltage-current characteristics did not change with the wiring layout, and consequently the power remained the same).

Bibliography

[1] Federal Aviation Administration. Ac 120-38 - transport category airplanes cabin ozone concentrations. `http://www.faa.gov/regulations_policies/advisory_circulars/index.cfm/go/document.information/documentID/22760/`, 1980. [Online; accessed 7-August-2012].

[2] United States Environmental Protection Agency. Ground-level ozone standards designations. `http://www.epa.gov/ozonedesignations/`, 2012. [Online; accessed 7-August-2012].

[3] Thomas B. Bahder and Chris Fazi. Force on an asymmetric capacitor. Technical Report ARL-TR-XXX, Army Research Laboratory, March 2003.

[4] Thomas Townsend Brown. A method of and an apparatus or machine for producing force or motion. GB300311 (A), November 1928.

[5] Thomas Townsend Brown. Electrokinetic apparatus. US2949550, August 1960.

[6] Thomas Townsend Brown. Electrokinetic transducer. US3018394, January 1962.

[7] Francis X. Canning. Experimental findings of lifters, asymmetrical capacitor thrusters, and similar electrogravitic devices. In *42nd AIAA/ASME/SAE/ASEE Joint Propulsion Conference & Exhibit*, Sacramento, CA, July 2006. American Institute of Aeronautics and Astronautics.

[8] Francis X. Canning, Cory Melcher, and Edwin Winet. Asymmetrical capacitors for propulsion. Technical Report NASA/CR-2004-213312, National Aeronautics and Space Administration, October 2004.

[9] S. I. Cheng. The glow discharge as an advanced propulsion device. Technical Report AeroChem TP-33, Office of Naval Research, March 1961.

[10] Edward A. Christenson and Paul S. Moller. Ion-neutral propulsion in atmospheric media. *AIAA Journal*, 5(10):1768–1773, October 1967.

[11] Dorian F. Colas, Antoine Ferret, David Z. Pai, Deanna A. Lacoste, and Christophe O. Laux. Ionic wind generation by a wire-cylinder-plate corona discharge in air at atmospheric pressure. *Journal of Applied Physics*, 108(103306), 2010.

[12] P. Cooperman. A theory for space-charge limited currents with application to electrical precipitation. In *AIEE Trans.*, pages 47–50, March 1960.

[13] Hans Fantel. Major de seversky's ion-propelled aircraft. *Popular Mechanics*, August 1964.

[14] Alexander Fridman and Lawrence A. Kennedy. *Plasma Physics and Engineering*. Taylor & Francis, 29 West 35th St New York, NY 10001-2299, 2004.

[15] M. Goldman, A. Goldman, and R. S. Sigmond. The corona discharge, its properties and specific uses. *Pure & Applied Chemistry*, 57(9):1353–1362, 1985.

[16] C. Kim, D. Park, K. C. Noh, and J. Hwang. Velocity and energy conversion efficiency characteristics of ionic wind generator in a multistage configuration. *Journal of Electrostatics*, 68:36–41, 2010.

[17] M Laroussi, K H Schoenbach, U Kogelschatz, R J Vidmar, S Kuo, M Schmidt, J F Behnke, K Yukimura, and E Stoffels. Current applications of atmospheric pressure air plasmas. In K H Becker, U Kogelschatz, K H Schoenbach, and R J Barker, editors, *Non-Equilibrium Air Plasmas at Atmospheric Pressure*, Series in Plasma Physics, chapter 9, pages 537–672. Institute of Physics Publishing, Bristol and Philadelphia, 2005.

[18] William M. Miller, Paul B. Miller, and Timothy J. Drummond. Force characterization of asymmetrical capacitor thrusters in air. In Marc G. Millis and Eric W. Davis, editors, *Frontiers of Propulsion Science - Progress in Astronautics and Aeronautics, Volume 227*, chapter 8, pages 293–327. American Institute of Aeronautics and Astronautics, New York, 2009.

[19] United States Department of Labor Occupational Safety & Health Administration. Chemical sampling information – ozone. `http://www.osha.gov/dts/chemicalsampling/data/CH_259300.html`, 2007. [Online; accessed 7-August-2012].

[20] Joseph Payton. Electrohydrodynamic propulsion. Fourth-year undergraduate project under advisor Prof Barrett, May 2010.

[21] Matthew Rickard, Derek Dunn-Rankin, Felix Weinberg, and Fred Carleton. Characterization of ionic wind velocity. *Journal of Electrostatics*, 63:711–716, 2005.

[22] M. Tajmar. Biefeld-brown effect: Misinterpretation of corona wind phenomena. *AIAA Journal*, 42(2):315–318, February 2004.

[23] R. L. Talley. Twenty first century propulsion concept. Technical Report PL-TR-91-3009, Phillips Laboratory, May 1991.

[24] A. M. Tyndall and G. C. Grindley. The mobility of ions in air. *Proceedings of The Royal Society A*, 110(754):341–364, February 1926.

[25] Jack Wilson, Hugh D. Perkins, and William K. Thompson. An investigation of ionic wind propulsion. Technical Report NASA/TM-2009-215822, National Aeronautics and Space Administration, December 2009.

[26] L. Zhao and K. Adamiak. Ehd gas flow in electrostatic levitation unit. *Journal of Electrostatics*, 64:639–645, 2006.

[27] Ch-47c chinook. `http://www.globalsecurity.org/military/systems/aircraft/ch-47c.htm`, 2012. [Online; accessed 23-August-2012].

[28] Lt. Col. Scott T. Davids, USMC. Telephone interview, 2012. [23-August-2012].